Title

Soot-particle core-shell and fractal structures from small-angle X-ray scattering measurements in a flame

Authors

Michelsen, Hope A
Campbell, Matthew F
Johansson, K Olof
et al.

Publication Date

2022-08-01

DOI

10.1016/j.carbon.2022.05.009

Soot-Particle Core-Shell and Fractal Structures from Small-Angle X-Ray Scattering Measurements in a Flame

Hope A. Michelsen,[*,†,‡] *Matthew F. Campbell,*[‡,§] *K. Olof Johansson,*[‡,∥] *Ich C. Tran,*[⊥,¶] *Paul E. Schrader,*[‡] *Ray P. Bambha,*[‡] *Emre Cenker,*[#,‡] *Joshua A. Hammons,*[⊥] *Chenhui Zhu,*[○] *Eric Schaible,*[○] *and Anthony van Buuren*[*,⊥]

[†]Department of Mechanical Engineering and Environmental Engineering Program, University of Colorado Boulder, Boulder, CO 80309 USA

[‡]Combustion Research Facility, Sandia National Laboratories, Livermore, CA 94550 USA

[§]Now at Department of Mechanical Engineering and Applied Mechanics, University of Pennsylvania, Philadelphia, PA 19104 USA

[∥]Now at KLA Corporation, Milpitas, CA 95035 USA

[⊥]Nanoscale Synthesis and Characterization Laboratory, Lawrence Livermore National Laboratory, Livermore, CA 94550 USA

[¶]Now at Irvine Materials Research Institute, University of California Irvine, Irvine, CA 92697 USA

[#]Now at R&DC, Saudi Aramco, Dhahran, 31311, KSA

°Advanced Light Source, Lawrence Berkeley National Laboratory, Berkeley, CA 94720 USA

*Corresponding Authors: Hope.Michelsen@colorado.edu; vanbuuren1@llnl.gov.

Keywords. SAXS, Soot, Surface-fractal, Mass-fractal, Core-Shell, Flame

ABSTRACT. We have characterized soot particles measured *in situ* in a laminar co-flow ethylene-air diffusion flame using small-angle X-ray scattering (SAXS). The analysis includes temperature measurements made with coherent anti-Stokes Raman spectroscopy (CARS) and complements soot volume-fraction and maturity measurements made with laser-induced incandescence (LII). We compared the results of fits to the SAXS measurements using a unified model and a fractal core-shell model. Power-law parameters yielded by the unified model indicate that aggregates of primary particles are in the mass-fractal regime, whereas the primary particles are in the surface-fractal regime in the middle of the flame. Higher and lower in the flame, the primary-particle power-law parameter approaches 4, suggesting smooth primary particles. These trends are consistent with fits using the fractal core-shell model, which indicate that particles have an established core-shell structure in the middle of the flame and are internally homogeneous at higher and lower heights in the flame. Primary-particle size distributions derived using the fractal core-shell model demonstrate excellent agreement with distributions inferred from transmission electron microscopy (TEM) images in the middle of the flame. Higher in the flame, a second small mode appears in the size distributions, suggesting particle fragmentation during oxidation. Surface oxidation would explain (1) aggregate fragmentation and (2) loss of core-shell structure leading to smoother primary-particle surfaces by removal of carbon overlayers. SAXS measurements are much more sensitive to incipient and young soot

particles than LII and demonstrate significant volume fraction from particles low in the flame where the LII signal is negligible.

1. INTRODUCTION

Soot is a toxic and environmentally destructive byproduct of incomplete combustion and pyrolysis of hydrocarbons. It has been linked to increased rates of morbidity and mortality from cancer and cardiovascular, pulmonary, and neurological illnesses [1-5]. Soot is also a very potent contributor to climate change and air pollution [6, 7]. There is hope that gaining a better understanding of soot formation and chemistry may enable new approaches to mitigating its emissions.

Incipient soot particles, produced in the first phase of soot formation, are largely composed of polycyclic aromatic hydrocarbons (PAHs) clustered together to form small (<~6 nm) [8-12], nearly spherical particles with disordered fine structure [13, 14]. As these particles age in the combustor, they lose hydrogen; their fine structure becomes more ordered, and they grow substantially in size and start to aggregate [14, 15]. Mature soot particles are composed of spherical or semi-spherical primary particles that have diameters in the approximate range of 10-50 nm [13, 14, 16-18]. These primary particles are tightly bound into secondary particles, dendritic aggregates with characteristic sizes on the order of 100 nm and larger. Mature primary particles are predominantly composed of graphite-like crystallites aligned parallel to the particle surface. The central region of these particles is typically randomly ordered [14]. This disordered region is on the order of 1-6 nm [19-23]. The near-surface crystallites are 4-10 layers thick and $\geq$ ~1 nm in length and width [24-28].

Despite decades of research on soot, the mechanisms responsible for soot formation are poorly understood. Gaps in the understanding of these processes stem largely from the paucity of experimental techniques that can provide information about particle evolution without perturbing the environment in which they are formed [14].

There have been many studies in which SAXS was used to measure particle sizes in flames [29-44] and in explosion-detonation fronts [45-47]. In such studies, a collimated beam of monochromatic hard X-ray photons is passed through the flame or detonation front, and forward-scattered photons are collected as a function of scattering angle on a position-sensitive detector downstream of the flame. Light-scattering models and approximations are used to extract information about the scattering population. The most commonly used model in studies of soot in flames is the so-called unified model [31, 35-37, 39-44, 48]. This model describes the SAXS signal over a range of sizes and morphologies with a combination of Guinier exponential and power-law functions [49-51]. The unified model does not explicitly provide information about the internal structure of the primary particles. Soot particles develop a core-shell structure as they evolve and mature, and it may be possible to extract information about the growth and maturation process using SAXS measurements and a model that accounts for this core-shell structure.

We collected SAXS data along the centerline of a sooting, partially premixed, ethylene-air diffusion flame, in which measurements were made previously of temperature using coherent anti-Stokes Raman spectroscopy (CARS), volume fraction and optical properties using laser-induced incandescence (LII) and laser extinction, and surface maturity using X-ray photoelectron spectroscopy (XPS) [52-54]. We analyzed the SAXS data using two types of models. We used a multi-mode unified equation to fit the data, assuming a mode for the primary particles and a

mode for the soot aggreges. We also used a core-shell fractal aggregate model that explicitly accounts for the density differences between the disordered core and the turbostratic shell of the primary particles and the fractal structure of the aggregates. The results from the different models were compared with each other, with primary-particle sizes from TEM data, and with soot-volume fractions from LII measurements.

SAXS-inferred volume fractions reach a maximum at a lower height in the flame than those measured using LII; this observation is consistent with X-ray scattering from young, internally disordered, hydrocarbon particles for which LII lacks sensitivity. The SAXS data indicate that, once mature, soot aggregates can be described as mass fractals whereas the primary particles that make up the soot aggregates are more appropriately described as surface fractals with rough surfaces. As we show in the present paper, SAXS can additionally provide information about the core-shell internal structure of the primary particles, either via the surface-fractal dimension, a measure of the surface roughness or surface area of a dense object [54], or explicitly using a model that accounts for the density differences between the disordered core and the turbostratic shell.

2. EXPERIMENTAL METHODS

2.1 Beamline. We performed SAXS measurements at Beamline 7.3.3 at the Advanced Light Source (ALS) synchrotron facility at Lawrence Berkeley National Laboratory. A paper by Hexemer *et al. [55]* provides details of the beamline setup. A detailed description of the experimental flame setup is provided by Michelsen *et al*. [56]. Only a brief description is provided here.

The beam of 10-keV (1.24-Å) X-ray photons has a flux of ~1.3×10^{12} photons/s and a beam size of ~500×400 μm^2 (W×H) at the location of the sample (i.e., flame) and is approximately 90% horizontally polarized. The burner and flame can be translated vertically and horizontally relative to the X-ray beam. On the downstream side of the flame, the scattered photons and collimated beam enter an evacuated flight tube through a Kapton polyimide film (DuPont) window. At the end of the flight tube, the scattered photons pass through a second Kapton film before reaching the two-dimensional detector (Dectris Ltd. model Pilatus 2M). The distance between the center of the flame and the detector for these studies was d = 1314 mm, which yielded a q range of approximately 0.017 - 0.57 Å^{-1}. This detector distance was chosen to optimize measurements in the q range of 0.1 – 0.6 Å^{-1}, which corresponds to characteristic length scales of 1 – 6 nm, the size range of both incipient-soot particles and internal core-shell structures of mature-soot particles. Exposure times were 300 seconds for each position in the flame.

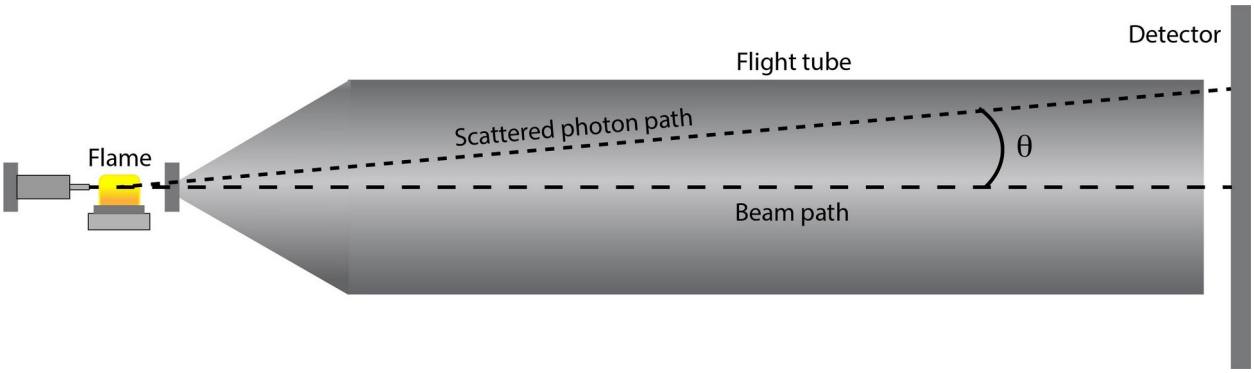

Figure 1. Experimental geometry. The X-ray beam travels from left to right on this figure and is indicated by the dashed line. An example trajectory of scattered photons is represented by the dotted line. The angle between them is θ.

With the scattering angle θ defined as shown in Fig. 1, the momentum transfer q is given by

$$q=\frac{4\pi}{\lambda}\sin\left(\frac{\theta}{2}\right)=\frac{2\pi}{L}\,, \qquad (1)$$

where λ is the wavelength of incident photons (1.24 Å), $\theta = \tan^{-1}\left(\frac{r}{d}\right)$ is the scattering angle for a photon hitting the detector a distance r from the X-ray beam (d is the distance between the center of the flame and the detector beam stop) [36, 37, 40]. The scattering angle is inversely related to the size of the particles and structures observed, and the Fourier length L represents the characteristic size of particles leading to scattering at angle θ [36, 40].

2.2 Burner and Flames. We performed experiments using a linear Hencken-type burner, which produces partially-premixed laminar co-flow diffusion flames that are ~3 mm wide and ~38 mm long [52]. The burner consists of a row of 25 small-gauge fuel tubes (each with an inside diameter of 508 μm) surrounded by hexagonal mesh 25 mm wide × 50 mm long for the co-flow of air. We recorded SAXS data along the long axis of the flame to minimize the relative contributions to the signal from flame edges, thus providing better comparisons with point measurements inside the flame from LII and CARS and simplifying the background subtraction and particle signal analysis.

Scattering from particles at the front and rear of the flame produces some uncertainty in the exact scattering length (d_{cm} = 131.4±1.9 cm) and q ($\frac{\Delta q}{q} \leq \pm 1.5\%$). This smearing effect results in ~1 Å (0.1 nm) uncertainty in the particle sizes reported here. Because the flame length changes with height above the burner, however, this smearing effect is not accounted for in the data modeling. The change in flame length with flame height is discussed in Michelsen *et al*. [56].

The flow rate of ethylene, the fuel, was 0.200 standard liters per minute (SLM), calibrated relative to standard conditions of 0°C and 1 atm, and the flow of air was 14.0 SLM. These flow conditions produce a flame known as Flame E1 in previous publications [52]. There are three

sets of measurements described in this analysis. They were recorded on different days. In this paper, we refer to these datasets as Flame E1a, Flame E1b, and Flame E1c. Mass flow controllers (MKS Instruments, Inc. Model GM50A) were calibrated (using a Sierra Instruments, Inc. Model SL-500) prior to use. Research-grade ethylene was supplied by Airgas, Inc. and was filtered (Swagelok Model SS-4F-05) immediately upstream of the mass flow controllers. House air was dried (Parker Hannifin Corp. Model IT0030-35) and passed through a carbon filter (Parker Hannifin Corp. Model 2002N-0A0-000/CI100-12-000) to remove hydrocarbons prior to entering the mass flow controller. The burner was maintained at a temperature of ~20°C by circulating cooled distilled water from a chiller (NESLAB Instruments, Inc. Model RTE-111) to the burner. The burner and flame were enclosed in an acrylic box to capture exhaust and prevent flame fluctuations produced by room-air currents; this setup, including the burner and enclosure, was attached to the beamline's remotely controlled *X-Z* stage to allow for translation of the flame in the beam.

2.3 Microscopy. We extracted soot samples from the flame using a sampling procedure described by Johansson *et al*. [53] and Michelsen *et al*. (submitted to *Proc. Combust. Inst.*). A tiny jet of N_2 was directed across the short axis of the flame. The N_2 jet and advected flame sample were captured by another probe connected to a slightly evacuated collection cell holding 3.05-mm-diameter copper mesh grids (Ted Pella #01824 and #01830) on which the soot samples were collected. Samples were collected at heights above the burner (HABs) of 3 mm, 4 mm, 5 mm, 6 mm, 7 mm, 8 mm, and 9 mm. TEM images were recorded for these samples using a JEOL USA, Inc. Model JEM-1200EX microscope, which was fitted with an eleven-megapixel digital camera (Gatan, Inc. model ES1000W). Most images were taken at 250,000-times magnification.

To infer primary-particle sizes from TEM micrographs, we implemented a MATLAB-based semi-automated process by adapting original software developed by Anderson *et al*. [57]. The methodology applied here is referred to as center-selected edge scoring (CSES). In this algorithm, the operator manually selects a point on the image that is judged to be the center of a primary particle. Given this center point and its neighboring pixels, the tool searches for the best-fit circles based on the intensity gradients. Further details about the primary-particle processing algorithm can be found in the paper by Anderson *et al*. [57]. When particles overlap along the line-of-sight in microscopy imaging, the overlapping area is darker than the non-overlapping region and can be erroneously detected as particles. Such artifacts were eliminated in the semi-automated process by the operator's judgement.

Prior to particle sizing, images were pre-processed to enhance the accuracy of the CSES algorithm and help the operator identify the centroids of primary particles. The pre-processing involves inversion, contrast enhancement, background subtraction, thresholding, and edge-preserved smoothing (e.g., median filtering). We analyzed more than 2100 primary particles to determine mean primary-particle sizes.

We examined soot-aggregate morphology by isolating and masking aggregates in the TEM images using ImageJ. We used these masked images to calculate the projected area A_{agg} and radius of gyration R_{g0} for each aggregate using Igor Pro (Version 8.04, WaveMetrics) [58], as described previously [59]. We corrected the values of R_{g0} for overlap between particles according to the recommendations of Brasil *et al*. [60], i.e., $R_g=(1-C_{ov})R_{g0}$. The primary-particle overlap coefficient C_{ov} is given by $C_{ov}=1.1(\ a_i + a_j - d_{ij})/(\ a_i + a_j) - 0.2$, where a_i and a_j are the radii of two primary particles, and d_{ij} is the distance between their centers [60, 61]. We calculated the number of primary particles per aggregate N_p from the projected aggregate area and the mean primary-

particle cross-sectional area $A_{pp\ [60\text{-}62]}$ and used these values of N_p in the derivation of the aggregate mass-fractal dimension D_f and fractal pre-factor k_g, i.e.,

$$N_p = k_a \left(\frac{A_{agg}}{A_{pp}} \right)^{\alpha_a} = k_g \left(\frac{R_g}{r'_{pp}} \right)^{D_f} \tag{2}$$

where $A_{pp} = \pi(r'_{pp})^2$, assuming a spherical shape, and r'_{pp} is the average primary-particle radius for each aggregate. The values for the projected-area pre-factor k_a and projected area exponent α_a depend on the overlap coefficient [60-62]. Fits to data provided in Brasil *et al*. [61] yielded the relationships $k_a = k_0 + k_1 C_{ov} + k_2 C_{ov}^2$, where k_0 = 1.10±0.01, k_1 = 0.270±0.182, and k_2 = 2.252±0.542, and $\alpha_a = \alpha_0 + \alpha_1 C_{ov}$, where α_0 = 1.080±0.003 and α_1 = 0.1854±0.0108. More details of these calculations are given in Section A of the supplementary material.

3. DATA ANALYSIS

3.1 Background Subtraction. The processing of the raw data and background subtraction approach are described in detail by Michelsen *et al*. [56]. The scattering signal recorded on the detector was azimuthally averaged using the Nika software (Release 1.74) [63], which yielded 1D profiles of scattering signal as a function of q. We normalized and background-corrected these profiles. Contributions to the uncorrected signal included flame-independent contributions from the instrument and background gas outside the flame and flame-dependent contributions from the temperature-varying and composition-varying combustion gases. We isolated and subtracted these contributions from the normalized signal. The SAXS data presented in this paper were processed used the scattering signal recorded at an HAB of 2 mm for the differenced signal, i.e., HAB0 = 2 mm (see [56] for details). These data are supplied as tabulated text and Excel files in the supplementary material. We used Igor Pro (Version 8.04, WaveMetrics) to fit

the background-subtracted scattering profiles using the models described in Sections 3.2 and 3.3. The data were fit in the range of 0.02 - 0.57 Å^{-1}, which corresponds to length scales of 1 - 30 nm.

3.2 Unified Fitting Method Assuming Homogeneous Primary Particles. We used the unified-fitting method [49-51, 64] to derive size and morphology information for the soot particles from the background-subtracted scattering profiles. This model is especially useful for examining hierarchical systems, such as soot aggregates of smaller primary particles. Different sizes of particles in the hierarchical structure are referred to as "modes". In the unified model, the contribution from each particle-size mode to the background-subtracted scattering signal is approximated by the sum of a Guinier exponential function and a structurally limited power-law function. Within each mode, scattering at the high-q values is fit using the power-law function, and scattering at the low-q values is fit using the exponential function. A typical two-mode function is given by [49, 50]

$$C\,I_{soot}(q) \approx P_{\psi}\left[G_{agg}\exp\left(\frac{-q^2R_g^2}{3}\right)+B_{agg}\exp\left(\frac{-q^2R_s^2}{3}\right)\left\{\frac{\left[\operatorname{erf}\left(\frac{qR_g}{\sqrt{6}}\right)\right]^3}{q}\right\}^P+G_{pp}\exp\left(\frac{-q^2R_s^2}{3}\right)+B_{pp}\left\{\frac{\left[\operatorname{erf}\left(\frac{qR_s}{\sqrt{6}}\right)\right]^3}{q}\right\}^{P_s}\right]+C_0 \quad (3)$$

where $I_{soot}(q)$ is the soot-scattering efficiency (i.e., the scattering intensity from soot, normalized by the beam intensity); C is an instrument-calibration constant, and C_0 is a small constant background; R_g is the radius of gyration of the aggregates, and R_s is the radius of gyration of the primary particles; P is the power-law parameter for the aggregates, and P_s is the power-law parameter for the primary particles.

The first and third terms on the right-hand side of this equation are expressions of the Guinier exponential function. The exponential (Guinier) pre-factors are [49, 50]

$$G_{agg}=C_e\acute{N}_{agg}n_{agg}^2=C_e\acute{N}_{agg}\rho_{eagg}^2V_{agg}^2 \quad (4)$$

and

$$G_{pp} = C_e \acute{N}_{pp} n_{pp}^2 = C_e \acute{N}_{pp} \rho_{epp}^2 V_{pp}^2 , \quad (5)$$

and their ratio provides an approximation for the number of primary particles per aggregate [35, 65], i.e.,

$$N_p = \frac{G_{agg}}{G_{pp}} . \quad (6)$$

In Eq. (4) and Eq. (5), $\acute{N}_{agg}$ is the average aggregate number density, and $\acute{N}_{pp}$ is the average primary-particle number density; n_{agg} is the number of electrons per aggregate, and n_{pp} is the number of electrons per primary particle; V_{agg} is the volume of the aggregate, and V_{pp} is the volume of the primary particle; ρ_{eagg} is the electron-density difference between the aggregate and the flame gases, and ρ_{epp} is the electron-density difference between the primary particle and the flame gases. Because the electron density is much larger in the particle than in the gas phase, we can assume that $\rho_{eagg} \cong n_{agg}/V_{agg}$ and $\rho_{epp} \cong n_{pp}/V_{pp}$. The constant C_e encompasses the instrument-calibration constant C, the single-electron scattering efficiency $I_e(q)$, and the detection volume V_{scat} (7.6×10^{-3} cm^3 in our case), i.e., [66, 67].

$$C_e = \frac{C I_e(q) V_{scat}}{P_\psi} = C r_0^2 d_{cm}^{-2} V_{scat} , \quad (7)$$

where d_{cm} is the distance to the detector in cm, and P_ψ is a polarization-correction term. The classical Thomson electron radius (i.e., Thomson scattering length) [68] r_0 is given by $r_0 = \frac{e^2}{m c^2}$ [69], where e is the charge of an electron (1.602177×10^{-19} C); m is the mass of an electron (9.1093836×10^{-28} g), and c is the speed of light (2.9979246×10^{10} cm/s), such that r_0=2.81794×10^{-13} cm, and the differential Thomson cross section for a free electron [67] is r_0^2 =7.94079×10^{-26} cm^2. Beamline 7.3.3 at the ALS is approximately 90% horizontally polarized

(the plane of polarization is defined by an azimuthal angle ψ of 90°); the polarization correction is derived in Section B of the supplementary material and is given by

$$P_{\psi}=\pi\left(1+\cos^{2}\theta\right). \tag{8}$$

The q dependence of the polarization correction is small (<0.5% deviation from unity for our experiment) and can be included in either the integration of the 2D images of the raw data or in the fit.

The second and fourth terms in Eq. (3) are expressions of the power-law function. The constant pre-factors for these terms depend on the type of power-law function observed. The power-law function can be used to define the following regimes observed in our results:

1. The Porod regime ($P_s = 4$) [70, 71],
2. The surface-fractal regime ($3 < P_s < 4$) [42, 50, 71-73], and
3. The mass-fractal regime ($P \leq 3$) [50, 71, 74].

In our study, the primary particles are associated with the Porod-law and surface-fractal regimes, as demonstrated in Section 4.4, and the aggregates are in the mass-fractal regime, as demonstrated in Section 4.3.

Low in the flame (during particle formation) and high in the flame (during particle oxidation), the primary particles meet the Porod condition, i.e., $P_s = 4$, indicating that the surfaces are distinct and smooth. Under these conditions [35, 49],

$$B_{pp}\left(P_s=4\right)=2\pi\frac{G_{pp}}{V_{pp}^{2}}S_{pp}\,, \tag{9}$$

where S_{pp} is the average primary-particle surface area. For primary particles in the middle of the flame, we have the conditions that $3 < P_s < 4$, and thus the power-law parameter P_s is related to

the mass-fractal dimension of the primary particle, D_{fs}, and surface-fractal dimension, D_s, such that $P_s = 2D_{fs} - D_s$ [42, 50, 72, 73], and [50, 72, 73]

$$B_{pp}(3<P_s \le 4)=\pi \frac{G_{pp}}{V_{pp}^2} S_{pp} \frac{\Gamma(P_s-1)\sin\frac{\pi(P_s-3)}{2}}{P_s-3}, \tag{10}$$

where Γ represents the gamma function. Equation (10) reduces to Eq. (9) for a spherical particle with $P_s = 4$. Assuming a spherical shape for the primary particles, the average primary-particle diameter ($\acute{d}_{pp}$ in nm) can be derived according to

$$\acute{d}_{pp}(3<P_s \le 4)=\frac{\sqrt{6}}{10}\left[\frac{G_{pp}}{B_{pp}} \frac{\Gamma(P_s-1)\sin\frac{\pi(P_s-3)}{2}}{P_s-3}\right]^{\frac{1}{4}}. \tag{11}$$

Alternatively, assuming a spherical shape, $\acute{d}_{pp}$ can be derived from the primary-particle radius of gyration (R_s in Å) according to [65, 75]

$$\acute{d}_{pp}=\sqrt{\frac{5}{3}}\frac{2R_s}{10}=\frac{R_s}{\sqrt{15}}. \tag{12}$$

In either case, the primary-particle volume V_{pp} is derived from the particle diameter, i.e.,

$$V_{pp}=\frac{\pi \acute{d}_{pp}^3}{6}. \tag{13}$$

In the mass-fractal regime ($P \le 3$, $P = D_f$) [50, 74],

$$B_{agg}(P \le 3)=G_{agg}\frac{P\Gamma\left(\frac{P}{2}\right)}{R_g^P}. \tag{14}$$

For mass-fractal aggregates, the ratio G_{agg}/B_{agg} provides an estimate of R_g. Solving Eq. (14) for R_g gives

$$R_g=\left[\frac{G_{agg}}{B_{agg}} P\Gamma\left(\frac{P}{2}\right)\right]^{\frac{1}{P}}. \tag{15}$$

If the calibration factor C is known, a volume fraction for soot in the flame can be inferred from the SAXS signal. The volume fraction is given by

$$V_f = V_{pp}\frac{G_{pp}}{Cr_0^2 d_{cm}^{-2} V_{scat} n_{pp}^2} = V_{pp}\frac{G_{pp}}{C_e n_{pp}^2} \tag{16}$$

The number of electrons per primary particle n_{pp} can be derived according to

$$n_{pp} = V_{pp}\frac{\rho_{pp}}{W} N_a n_{atom}\,, \tag{17}$$

where ρ_{pp} is the density of the primary particle; W is the average atomic weight of the atoms in the primary particle; N_a is Avogadro's number (6.02214×10^{23} mol^{-1}), and n_{atom} is the average number of electrons per atom. The value for n_{atom} can be approximated relative to the estimated carbon-to-hydrogen (C/H) ratio according to

$$n_{atom} = \frac{n_c\frac{C}{H} + n_H}{\frac{C}{H} + 1}\,. \tag{18}$$

where n_{C} is the number of electrons per carbon atom (6), and n_{H} is the number of electrons per hydrogen atom (1). We estimated the C/H ratio as a function of HAB based on measurements of the dispersion exponent inferred from LII measurements between HABs of 4 and 9 mm [53] and the relationship between the C/H ratio and dispersion exponent ξ given by [76]

$$\frac{C}{H} = \left[(0.39\pm0.02)\xi - (0.27\pm0.03)\right]^{-1}. \tag{19}$$

The ratio of density to atomic weight in Eq. (17) can be replaced by the inverse of the average atomic molar volume V_M, which is relatively constant over a wide range of hydrocarbon composition but varies with temperature according to [76]

$$V_M(T) = V_M(T_{\text{st}})\left[1 + \alpha_{TE}(T - T_{\text{st}})\right]^3, \tag{20}$$

where the standard temperature T_{st} is 298.15 K; $V_M(T_{st})$ is 5.91 cm^3/mol; the linear thermal expansion coefficient α_{TE} is 2.163×10^{-5} K^{-1} [76], and T is the flame temperature. The number of electrons per particle can thus be expressed as

$$n_{pp}=V_{pp}\frac{N_a}{V_M}\left(\frac{6\frac{C}{H}+1}{\frac{C}{H}+1}\right), \tag{21}$$

and the electron density can similarly be expressed as

$$\rho_{epp}=\frac{N_a}{V_M}\left(\frac{6\frac{C}{H}+1}{\frac{C}{H}+1}\right), \tag{22}$$

for a known value of C/H ratio.

In regions of the flame where a single-mode model was adequate to describe the data, and the two-mode model did not converge, we fit the data using a single-mode equation, i.e.,

$$C\,I_{soot}\approx P_{\psi}\left[G_1\exp\left(\frac{-q^2R_1^2}{3}\right)+B_1\left\{\frac{\left[\operatorname{erf}\left(\frac{qR_1}{\sqrt{6}}\right)\right]^3}{q}\right\}^{P_1}\right]+C_0, \tag{23}$$

where R_1 is the radius of gyration, and P_1 is the power-law parameter. For these fits, the exponential and constant pre-factors are

$$G_1=C_e\acute{N}_1n_1^2=C_e\acute{N}_1\rho_{e1}^2V_1^2 \tag{24}$$

and

$$B_1(P_1\le 3)=G_1\frac{P_1\Gamma\left(\frac{P_1}{2}\right)}{R_1^{P_1}} \tag{25}$$

when $P_1 \le 3$, and

$$B_1(3<P_1\le 4)=\pi\frac{G_1}{V_1^2}S_1\frac{\Gamma(P_1-1)\sin\frac{\pi(P_1-3)}{2}}{P_1-3} \tag{26}$$

when $3 < P_1 \leq 4$. $\acute{N}_1$ is the average particle number density; n_1 is the number of electrons per particle; V_1 is the volume per particle; S_1 is the particle surface area, and the electron density difference between the particle and the gas is $\rho_{e1} \cong n_1/V_1$. For $P_1 \leq 3$, we calculated the average primary-particle diameter $\acute{d}_1$ by combining Eq. (25) and Eq. (12), i.e.,

$$\acute{d}_1(P_1 \leq 3) = \frac{1}{\sqrt{15}}\left[\frac{G_1}{B_1} P_1 \Gamma\left(\frac{P_1}{2}\right)\right]^{\frac{1}{P_1}}. \tag{27}$$

For $P_1 > 3$, we used the relationship for the surface-fractal regime, i.e.,

$$\acute{d}_1(3 < P_1 \leq 4) = \frac{\sqrt{6}}{10}\left[\frac{G_1}{B_1} \frac{\Gamma(P_1 - 1)\sin\frac{\pi(P_1 - 3)}{2}}{P_1 - 3}\right]^{\frac{1}{4}}. \tag{28}$$

We used Eq. (13) combined with Eq. (16) to calculate volume fractions.

Analysis of the TEM images from this flame demonstrates that the primary-particle sizes at each flame location can be represented by a log-normal distribution. This observation is consistent with previous studies of monomers [77, 78] and aggregated primary particles [79-81]. For comparisons with primary-particle size distributions inferred from TEM images, we derived log-normal distributions from the results of the unified fits. The normalized log-normal distribution $G(r_{pp})$ is expressed as

$$G(r_{pp}) = \frac{1}{\sqrt{2\pi}\, r_{pp} \ln \sigma_{pp}} \exp\left[\frac{-\ln^2\left(\frac{r_{pp}}{r_0}\right)}{2\ln^2(\sigma_{pp})}\right], \tag{29}$$

where r_0 is the geometric mean (i.e., median) of the distribution, and σ_{pp} is the geometric standard deviation. From the work of Beaucage *et al*. [82], the natural log of σ_{pp} can be calculated according to

$$\ln \sigma_{pp} = \frac{1}{2\sqrt{3}}\left(\ln \frac{R_s^4 B_{pp}}{1.62 G_{pp}}\right)^{\frac{1}{2}}. \tag{30}$$

The median primary-particle radius r_0 can be inferred from

$$r_0 = \left(\frac{10}{2}\right) \acute{d}_{pp} \exp\left[\frac{-\ln^2(\sigma_{pp})}{2}\right], \tag{31}$$

where $\acute{d}_{pp}$ is the average primary-particle diameter in nm, as given in Eq. (11). Equation (31) differs from the equation given in Beaucage *et al*. [82] for r_0, which appears to be incorrect and yields solutions that are very far from those of the TEM images or the fractal core-shell model.

The bimodal unified model has 9 adjustable parameters, and the single-mode unified model has 5 adjustable parameters. These parameters are summarized in Table 1.

Table 1. Summary of adjustable parameters in unified-fit and fractal core-shell models.

Single-mode unified-fit	Bimodal unified-fit	Fractal core-shell	Bimodal fractal core-shell	Bimodal core-shell
	G_{agg}	K_{pp}	K_{pp}	K_{pp}
	R_g	R_g	R_g	
	P	D_f	D_f	
	B_{agg}	γ	γ	
P_1	P_s	t	t	t
R_1	R_s	r_0	r_0	r_0
G_1	G_{pp}	σ_{pp}	σ_{pp}	σ_{pp}
B_1	B_{pp}		K_{small}	K_{small}
			r_{0small}	r_{0small}
			σ_{small}	σ_{small}
C_0	C_0	C_0	C_0	C_0

At most HABs, the data are best fit with the bimodal unified model. Fits with the bimodal unified model fail to converge for low HABs, where aggregates have not formed, and for high HABs, where aggregates have fragmented during oxidation. For these HABs, the single-mode unified model was used.

At all HABs the value of C_0 is negligible as a result of the background-subtraction process applied to the raw data [56]. The primary-particle mode of the bimodal unified model is well constrained by the data. Because the q range was limited to values $\geq$ 0.02 Å^{-1}, fits for the aggregate mode are less well constrained, and aggregate parameters have larger uncertainties.

3.3 Model for Fractal Aggregates with Core-Shell Primary Particles. The first particles produced during the formation of soot are small (<~6 nm) [8-12] and disordered [13, 14] and have elemental carbon-to-hydrogen (C/H) ratios in the range of 1.4-2.5 [14, 76, 83-89]. As these particles grow and evolve to mature primary particles, they accumulate layers of turbostratic graphite with crystallites aligned parallel to the particle surface. Mature-soot primary particles have C/H ratios of 8-20 [14, 76, 83, 84, 87, 89] and a core-shell structure with disordered core regions of 1-6 nm [19-23], surrounded by turbostratic graphite crystallites that are 4-10 layers thick and $\geq$ ~1 nm in length and width [24-28]. In addition to fitting our data using Eq. (3), we performed fits to the data with a model that explicitly accounts for this core-shell structure of mature or partially mature soot particles.

We fit the data using the following expression for scattering efficiency of a bimodal distribution of particles:

$$C\,I_{core-shell}(q) = K_{pp} P_{\psi} V_{pp} P(q) S(q) + K_{small} P_{\psi} V_{small} P_{small}(q) + C_0, \quad (32)$$

where $P(q)$ is a function of the primary-particle form factor ($F(q)$) [90] and is itself sometimes referred to as the "primary-particle form factor" [71, 91, 92] or "primary-particle structure factor" [93, 94]; $S(q)$ is the aggregate structure factor, which describes interactions between the primary particles in the aggregate [50, 90, 94]; $P_{small}(q)$ is related to the form factor for a non-aggregated-monomer mode; V_{pp} is the volume for the primary particles; V_{small} is the volume for

the monomer-mode particles, and C_0 is a small constant background. The scaling constants for each mode are given by

$$K_{pp} = C_e \acute{N}_{ppCS}, \text{ and} \tag{33}$$

$$K_{small} = C_e \acute{N}_{small}, \tag{34}$$

where $\acute{N}_{ppCS}$ is the average aggregated primary-particle number density, and $\acute{N}_{small}$ is the average monomer-mode-particle number density. The form factor is given as [93]

$$P(q) = \frac{1}{V_{pp}} \int_0^\infty G(r'_{pp}) F^2(q) \, d r'_{pp}, \tag{35}$$

where $G(r_{pp})$ is the probability distribution function for the primary-particle size; r_{pp} is the radius of the primary particle; r'_{pp} represents the integration variable, and $F(q)$ is the primary-particle form factor. If q is very small (i.e., if $q^{-1} >> r_{pp}$), $P(q) = 1$ [92]. For a core-shell primary particle that has a core volume of V_{core}, core radius of r_{core}, core electron density of ρ_{ecore}, and shell electron density of ρ_{eshell}, $F(q)$ can be expressed as [75, 91, 93, 95]

$$F(q) = \frac{3 V_{core} (\rho_{ecore} - \rho_{eshell}) j(q r_{core})}{(q r_{core})^3} + \frac{3 V_{pp} (\rho_{eshell}) j(q r_{pp})}{(q r_{pp})^3} . \tag{36}$$

To facilitate integration of Eq. (35) over a particle-size probability distribution, $F(q)$ can alternatively be written in terms of the primary-particle radius [93], i.e.,

$$F(q) = \frac{4\pi}{q^3} \left[(\rho_{ecore} - \rho_{eshell}) j(q r_{pp} - tq) + (\rho_{eshell}) j(q r_{pp}) \right], \tag{37}$$

where

$$j(x) = \sin x - x \cos x , \tag{38}$$

and t is the shell thickness, such that

$$r_{core} = r_{pp} - t . \tag{39}$$

The form factor for the monomer mode is expressed as

$$P_{small}(q)=\frac{1}{V_{small}}\int_0^{\infty} G\left(r'_{small}\right)F^2(q)\,d\,r'_{small}, \tag{40}$$

where $G(r_{small})$ is the probability-distribution function for the monomer-mode particle size; r_{small} is the radius of the monomer-mode particle; r'_{small} represents the integration variable, and $F_{small}(q)$ is the monomer-mode form factor. We assume that the monomer-mode particles are internally homogeneous and have an electron density the same as that of the core of the core-shell particles. The associated form factor is then expressed as

$$F_{small}(q)=\frac{4\pi}{q^3}\left[(\rho_{ecore})\,j(q\,r_{small})\right]. \tag{41}$$

The electron density for the primary-particle core and shell can be estimated using Eq. (22). We assumed that the core was similar in elemental composition to incipient particles with a C/H ratio of 2, and we assumed that the shell was similar in elemental composition to mature particles with a C/H ratio 8. These values yielded electron densities for the core of 442 nm^{-3} at 298 K and 396 nm^{-3} at 2000 K, and for the shell of 555 nm^{-3} at 298 K and 498 nm^{-3} at 2000 K. For reference, the electron density of graphite is 662 nm^{-3}, given a density for graphite at room temperature of 2.2 g/cm^3. These values are similar to values of 348 nm^{-3} for incipient-soot particles and 546 nm^{-3} for mature-soot particles used by Hessler *et al*. [96]. Yon *et al*. [97] used a value of 3.59 nm^{-3}, which is approximately two orders of magnitude smaller than those used here and by Hessler *et al*. [96].

We represented the probability-distribution function as a normalized log-normal distribution according to Eq. (29). The monomer mode was also assumed to be described by a log-normal size distribution, in which r_{small} replaces r_{pp}; r_{0small} replaces r_0, and σ_{small} replaces σ in Eq. (29).

Using the relationships given in Heinson *et al*. [92], the aggregate structure factor can be expressed in terms of D_f and R_g as

$$S(q)=1+\frac{\gamma}{R_g^{D_f}}\Gamma\left(\frac{D_f}{\gamma}\right)\left[\frac{\Gamma\left(\frac{D_f+2}{\gamma}\right)}{2\Gamma\left(\frac{D_f}{\gamma}\right)}\right]^{\frac{D_f}{2}}\int_0^{\infty}\left(r_{pp}^{'}\right)^{D_f-1}\exp\left[-\left(\frac{r_{pp}^{'}}{\zeta}\right)^{\gamma}\right]\frac{\sin\left(q\,r_{pp}^{'}\right)}{q\,r_{pp}^{'}}d\,r_{pp}^{'}, \tag{42}$$

where γ is the stretching exponent [92], and ζ is the cutoff parameter [92]. If γ =1, this expression can be integrated analytically; we have integrated this expression numerically, using γ as a fitting parameter and assuming that the cutoff parameter is given by [98]

$$\zeta=R_g\left[\frac{\Gamma\left(\frac{D_f+2}{\gamma}\right)}{2\,\Gamma\left(\frac{D_f}{\gamma}\right)}\right]^{\frac{1}{2}}. \tag{43}$$

In the discussion below, we refer to the model described by Eq. (32) as the "Bimodal Fractal Core-Shell (BiFCS) model". For locations in the center of the flame, the data were fit well without a monomer mode, and K_{small} tended toward zero. We refer to this model as the "Fractal Core-Shell (FCS) model". For the lowest HABs, the BiFCS model was not able to fit the data. For these locations, we were able to fit the data using a bimodal-monomer model that did not assume aggregation. In these cases, we assumed $S(q)$ = 1 but allowed one of the monomer modes to have a core-shell structure. We refer to this model as the "Bimodal Core-Shell (BiCS) model".

The volume fraction for the core-shell model V_{fCS} can be calculated from these results according to

$$V_{fCS}=\frac{K_{pp}V_{pp}+K_{small}V_{small}}{Cr_0^2d_{cm}^{-2}V_{scat}}=\frac{\left(K_{pp}V_{pp}+K_{small}V_{small}\right)}{C_e}. \tag{44}$$

where

$$V_{pp}=\frac{4\pi}{3}\int_0^{\infty}\left(r_{pp}^{'}\right)^3G\left(r_{pp}^{'}\right)d\,r_{pp}^{'}, \tag{45}$$

and

$$V_{small} = \frac{4\pi}{3} \int_0^{\infty} \left(r'_{small}\right)^3 G\left(r'_{small}\right) d\, r'_{small}. \quad (46)$$

Values of N_p were derived using Equation (2) with k_g given by [92]

$$k_g = \varphi \frac{\Gamma\left(\frac{D_f}{\gamma}\right)}{\gamma} \left[\frac{2\,\Gamma\left(\frac{D_f}{\gamma}\right)}{\Gamma\left(\frac{D_f+2}{\gamma}\right)} \right]^{\frac{D_f}{2}}, \quad (47)$$

where φ represents the packing fraction or packing density [92, 99], which was assumed to have a value of 0.36 for compact aggregates (HABs of $\leq$ 4 mm) [99] and a value of 0.68 for more mature aggregates [92].

The fractal core-shell model and the bimodal core-shell model each have 8 adjustable parameters, and the bimodal fractal core-shell model has 11 adjustable parameters. These parameters are summarized in Table 1.

The data at most HABs are best fit with the fractal core-shell model. Fits require the bimodal fractal core-shell model or bimodal core-shell model at low HABs, where particles are just forming, and require the bimodal fractal core-shell model at high HABs, where particles appear to be fragmenting during oxidation. The bimodal models account for primary-particle monomers just forming at low HABs and generated during oxidation at high HABs. Fits using the fractal core-shell model (neglecting primary-particle monomers) fail to converge at these HABs.

At all HABs the value of C_0 is essentially zero following the background-subtraction process described previously [56]. Parameters representing the primary particles are well constrained by the data. Parameters associated with the aggregates are less well constrained because of the limited range of q (0.02 – 0.57 Å^{-1} corresponding to 1-30 nm). Better assessment of aggregate

characteristics would be achieved with lower values of q, but our focus in this study was on smaller features for which the q range was optimized.

4. RESULTS AND DISCUSSION

4.1 General Trends. Figure 2a shows the total normalized signal for a range of HABs. The peak at q of 0.37 Å^{-1} is an interference from the Kapton window at the flight-tube entrance. Figure 2b shows the background-subtracted scattering profiles from Michelsen *et al*. [56]. The signal from soot increases with increasing HAB between 2 and 6 mm and then decreases with HAB. This trend is consistent with the measurements of mature-soot volume fraction made using LII calibrated with laser extinction [52, 53].

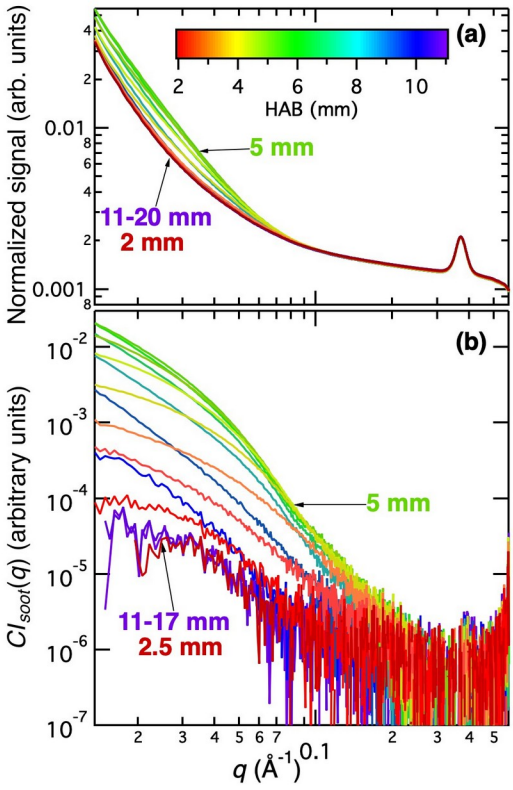

Figure 2. Scattering signal for a range of heights in the flame. The (a) total normalized signal and (b) background-subtracted signal, demonstrating contributions from soot, are shown as a

function of q for HABs between 2 mm and 17 mm for a single representative dataset (Flame E1b). Lines are color coded by HAB as indicated by the color scale in (a).

4.2 Particle Size. Figure 3a presents results from fits using the unified model for values of the radius of gyration for soot aggregates R_g (purple) and primary-particle diameter d_{pp} (green) from Eq. (3) and the monomodal radius of gyration (pink) from Eq. (23). The radius of gyration is indicated on the left axis, and the associated diameter (assuming spherical particles) is shown on the right axis. The results are plotted as a function of HAB. These results suggest that the aggregate radius of gyration increases with increasing height in the flame until ~5.5-6 mm at which point the particles stop growing. Between 3.75 mm and 5.5 mm, the radius of gyration increases by a factor of 58±27%. This change is attributable to the increase in size of the primary particles between 3.75 and 4.0 mm and the increase in number of primary particles per aggregate N_p of factors of ~6 between 3.75 and 5.5 mm, shown in Fig. 3b. The large uncertainties are likely partially attributable to the variability in aggregate size. In addition, the SAXS measurements did not sample small enough values in q to provide an accurate measure of the larger aggregate sizes; the error bars represent the standard deviation of the fit. Unfortunately, the number of aggregates sampled for TEM measurements was too small for a reliable estimate of aggregate parameters.

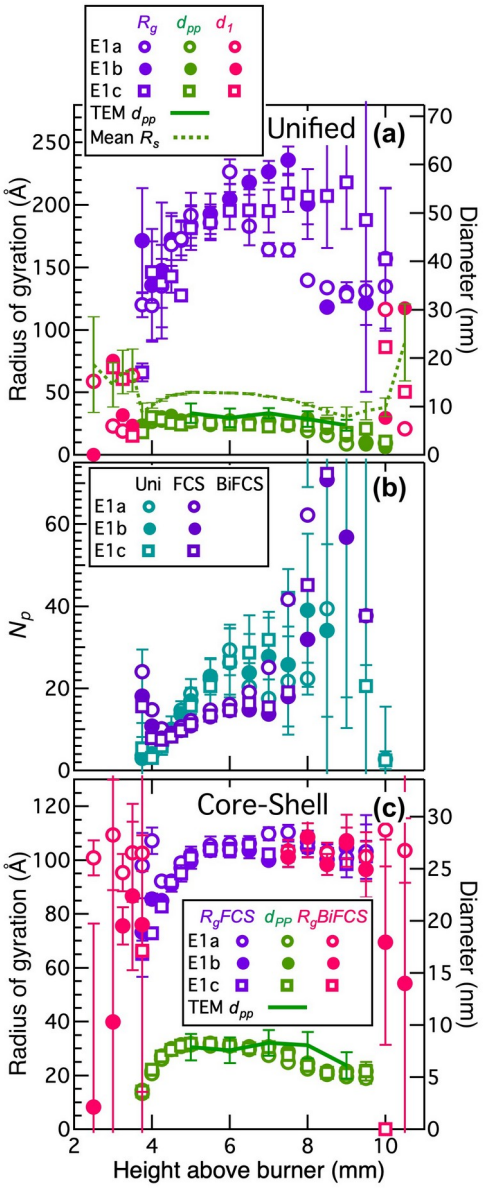

Figure 3. Radii of gyration, number of primary particles per aggregate, and primary-particle sizes derived from fits to scattering profiles. The ((a) and (b)) unified model and (c) fractal core-shell model were fit to three flame datasets assuming either two modes (purple and green points) or assuming a single mode (pink symbols). (a) Mean and (c) median primary-particle diameters (green symbols) are compared with (a) mean and (c) median primary-particle diameters from TEM analysis (green lines) (right axis). In (a), the green symbols were derived using Eqs. (11),

(27), and (28), and the dashed green line was derived using Eq. (12). In (b), the numbers of primary particles per aggregate from the unified model (blue-green symbols) are compared with values from the fractal core-shell model (purple symbols). Error bars represent the standard deviation of the fit to the SAXS data. Error bars for TEM values represent one σ standard deviation of the arithmetic mean values in (a) and geometric mean values in (c).

Results of fits using the fractal core-shell model also suggest that the radius of gyration of the aggregates, shown in Fig. 3c, increases with increasing HAB until ~5.5 mm. With the core-shell model, the increase in R_g between 3.75 mm and 5.5 mm is ~40%, which is within the large uncertainties of the increase inferred from the unified-fitting method. N_p also increases (see Fig. 3b), but this increase is difficult to assess because N_p was derived according to Eq. (47) assuming values of φ estimated from the literature. The weighted average radius of gyration from the fractal core-shell model is 104.4 ± 1.5 Å at an HAB of 5.5 mm, which is approximately 55% of the value of 188.3 ± 3.9 Å yielded by the unified-fitting method. These error bars represent precision error for the three measurements at each HAB. The error bars shown in Fig. 3 represent the estimated standard deviation from the fit provided by Igor Pro. Although the precision error demonstrates reasonable confidence in the fit, the systematic error is expected to be significant for size estimates of aggregates of this size over the q range sampled.

Figure 3a shows mean primary-particle diameters derived from the unified-fitting method compared with mean diameters inferred from TEM images, and Fig. 3c shows the corresponding comparison for median primary-particle diameters derived from the fractal core-shell model and TEM images. The primary-particle sizes derived from fits for both models increase between 3.75

mm and 4 mm, and, for the fractal core-shell model, they continue to increase until 5 mm; they are approximately constant in the HAB range of 5-6 mm, above which they decrease.

The values for primary-particle size for the unified-fitting method depend on whether they were derived using Eq. (12) (from the R_s produced by the fits) or using Eq. (11) (from the ratio of exponential and power-law pre-factors). Equation (11) yields values that are consistently lower than those from TEM measurements, and Eq. (12) gives values consistently higher than TEM values. In the range of HABs of 5-7 mm, the mean TEM value is 8.27 ± 1.67 nm; the mean value from Eq. (11) is 6.64 ± 0.35 nm, and the mean value from Eq. (12) is12.65 ± 0.36 nm. At low HABs, the unified model yields values of d_{pp} that depend on whether the particle is in the surface-fractal or mass-fractal regime. This observation may be attributable to the equations used to derive d_{pp} for the different regimes or may indicate a bimodal-monomer size distribution between 2.5 and 3.5 mm.

The fractal core-shell model results agree very well with median diameters derived from TEM images, as shown in Fig. 3c. For comparison, in the HAB range of 5-7 mm, the average value of the median of the primary-particle size distribution from the analysis of TEM images is 7.92±0.35 nm, whereas the average median from the SAXS data using the fractal core-shell model is 7.95±0.24 nm.

Figure 4 shows size distributions derived from the unified-fitting method using Eqs. (29), (30), and (31) (green lines) compared with size distributions inferred from TEM images at selected HABs. Representative examples of these TEM images are shown in Fig. 5. The size distributions retrieved using the unified-fitting method are consistently smaller than those extracted from TEM data. Median sizes from TEM data are 35±11% larger than those derived using the unified model over the HAB range of 5 – 7 mm.

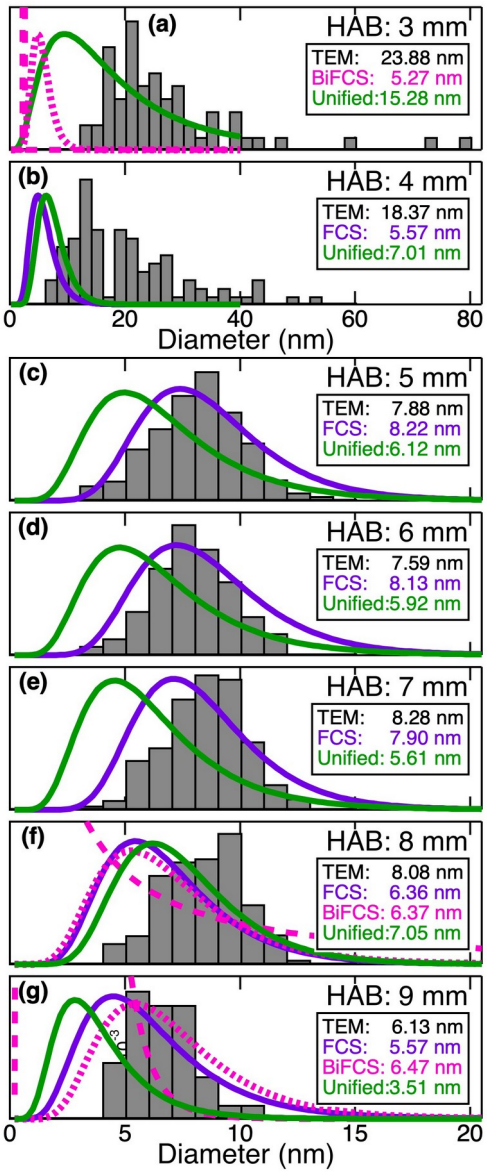

Figure 4. Primary-particle size distributions inferred from fits to SAXS data and TEM image analysis. Histograms derived from TEM data are shown for HABs of (a) 3 mm, (b) 4 mm, (c) 5 mm, (d) 6 mm, (e) 7 mm, (f) 8 mm, and (g) 9 mm. Solid purple lines show the results of fits using the fractal core-shell model; broken pink lines show the results of fits using the bimodal fractal core-shell model, and solid green lines show the results of fits using the unified model. The results are for fits to the data from Flame E1b. (a) and (b) have different scales on the x-axis than (c)-(g). Each panel lists median diameters inferred from TEM analysis and fits to the fractal

core-shell (FCS) model, bimodal fractal core-shell model (BiFCS, larger mode), and unified-fit model.

The size distributions derived using the fractal core-shell model demonstrate remarkably good agreement with the TEM values between 5 and 7 mm, as shown in Figs. 4c, 4d, and 4e; differences between them are not statistically significant. This model explicitly employs size distributions, rather than a single values of d_{pp}, to fit the X-ray scattering at each HAB. In addition to the excellent agreement in median sizes between the measurements and the FCS model (discussed above), there is very good agreement in the widths of the size distributions in this HAB range. TEM images of particles extracted from the flame in this HAB range (Figs. 5c, 5d, and 5e) show quasi-spherical primary particles bound into larger aggregates typical of mature soot particles.

At HABs between 3.75 and 9.5 mm, the data could be fit with a single-mode primary-particle size distribution at each HAB. At higher and lower HABs, bimodal primary-particle size distributions were necessary to fit the data. At HABs of 7.5 – 9.5 mm, the data could be fit with either a single-mode distribution or with a bimodal distribution. The results for both types of fits are shown in Figs. 4f and 4g. The bimodal model suggests rapid growth in number density of a mode of particles with median diameters of ~2 nm at HABs of 7.5 mm and above. This mode is consistent with fragmentation of particles during oxidation [97, 100-104]. Sarofim, Lighty, and coworkers [100, 101] first observed small-mode production during soot oxidation using electric-mobility analysis and attributed this mode to fragmentation and breakup of particles as they oxidize. Previous results suggest that, once the more ordered outer layers are removed, oxidation of the disordered core occurs rapidly [105, 106]. The TEM images at 9 mm demonstrate smaller

primary particles and significantly smaller aggregates (Fig. 5g), as would be expected for oxidized particles. The small (2-nm) mode is not apparent in the TEM images, but it is possible that the particle collection for the TEM analysis under sampled or missed these small-mode particles.

At lower HABs (3 – 4 mm), both models estimate particle sizes that are significantly smaller than those derived from the TEM images (factor of ~3.9 for the core-shell model and ~2.1 for the unified model), as shown in Figs. 4a and 4b. The corresponding TEM images, shown in Fig. 5a and Fig. 5b, demonstrate relatively large blobby particles. Condensation or adsorption and coagulation may have occurred during sampling for the TEM analysis, generating such particles. Alternatively, these particles may be present in the flame at concentrations too small to fit with confidence. In addition, the limited q range of this study hinders analysis of particles of this size, and the soot signal at low HABs is difficult to distinguish from the gas-phase signal [56], hindering retrieval of particle characteristics. The uncertainties are reflected in the error bars shown in Fig. 3 for particle sizes at these HABs.

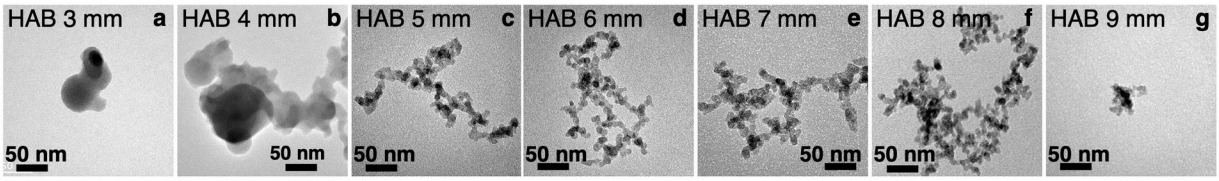

Figure 5. Representative TEM images of particles extracted at selected HABs. Images are shown for HABs of (a) 3mm, (b) 4 mm, (c) 5 mm, (d) 6 mm, (e) 7 mm, (f) 8 mm, and (g) 9 mm at 250,000x magnification from Flame E1.

The radii of gyration derived using the fractal core-shell model appear to be relatively large at HABs $\leq$ 4 mm. At HABs of 3.5 mm and lower, the fractal core-shell model failed to converge,

and the bimodal-monomer model (BiCS) was required. The results suggest a second mode with a diameter of ~2 nm in this region of the flame.

4.3 Aggregate Shape. Insight into particle shape is provided by the power-law parameters from the unified model and the mass-fractal dimension from the fractal core-shell model. The power-law parameter P gives information about the aggregate morphology and how this morphology changes as the particles evolve. In the mass-fractal regime ($P < 3$), P can be equated with the mass-fractal dimension D_f. The unified model produces values of P less than 3, which vary little with HAB at all HABs between 3.5 and 10 mm, as shown in Fig. 6a. Between 4.5 and 7.5 mm, the average value of P is 2.54±0.11. Figure 6b shows the mass-fractal dimension derived from fits using the fractal core-shell model. D_f derived with this model is also relatively constant with HAB with an average value of 2.21±0.11 between 4.5 and 7.5 mm.

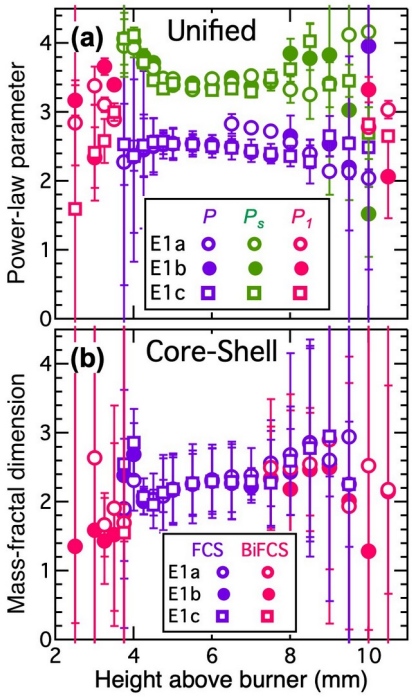

Figure 6. Power-law parameters and mass-fractal dimensions derived from fits to SAXS profiles. The (a) unified model and (b) fractal core-shell model were fit to three flame datasets assuming

either two modes (purple and green points) and using either (a) Eq. (3) or (b) Eq. (32) or assuming a single mode (pink symbols) and using (a) Eq. (23) or (b) Eq. (32) with $K_{small} = 0$. Power-law parameters are shown for the aggregate (purple symbols) and primary particles (green and pink symbols) in (a), and values for mass-fractal dimension for the aggregate (purple and pink symbols) are shown in (b). All error bars represent one σ standard deviation of the fit.

Although values of D_f inferred with the fractal core-shell model are lower than the values of P derived with the unified-fit model, both average values are much larger than the average given by TEM measurements of 1.65±0.30 in this HAB range. Previous work has demonstrated that mature-soot particles typically have mass-fractal dimensions in the range of 1.7-1.9 [62, 107-112], and LII measurements on the present flame indicate that the particles are mature at HABs of 5 mm and higher [53]. We would expect values of P and D_f from the SAXS measurements to be in the range of 1.7-1.9 at these HABs. The source of this significant discrepancy is likely attributable to the lack of data at small enough q values to capture the scattering behavior and retrieve the morphologies of particles in the aggregate size range.

4.4 Primary-Particle Shape and Internal Structure. In the range of HABs of 4.5 – 7.5 mm, the power-law parameter for the primary-particle mode P_s given by the unified model is approximately constant at a value of 3.44±0.09. Assuming that the primary particles are spherical ($D_f = 3$), homogeneous, and compact, the results yield a surface-fractal dimension D_s of 2.56±0.09 ($D_s = 2D_f - P_s$) [42, 72, 73], implying measurable surface roughness. A power-law parameter that approaches 4 is characteristic of a spatially homogeneous spherical object with a smooth surface, i.e., $D_s \cong 2$. A power-law parameter less than 4 is also consistent with scattering from non-spherical particles with smooth surfaces. A smooth oblate or prolate spheroid could

have a D_s of 2 with a P_s of 3 and a D_f of 2.5. A prolate spheroid is consistent with the development of necking or bridging between primary particles during aggregate formation and growth [16, 20, 62, 97, 103, 104, 113-115].

Values of P_s < 4 may also be consistent with the core-shell structure of the mature primary particle [116]. Figure 7 shows the ratio of the shell thickness to the primary-particle radius. A homogeneous particle would give a value of either one if the entire particle had the density of a mature soot particle or zero if the particle had the density of a young soot particle. In practice, the fits yielded results with reasonable error bars only in regions where a strong core-shell structure is expected. The results shown in Fig. 4 suggest that the core-shell structure is becoming established by ~4.25 mm. The core-shell structure appears to be stable between 5.0 and 6.5 mm with a shell thickness that is ~26% of the radius of the particle. The core diameter is ~6.0 nm, and the thickness is ~1.0 nm, i.e., ~4 turbostratic graphite layers, in this region of the flame. This structure is consistent with high-resolution TEM results showing mature soot particles with a disordered core of 1-6 nm in diameter [19-23] surrounded by more ordered turbostratic graphite crystallites 4-10 layers thick [26, 27].

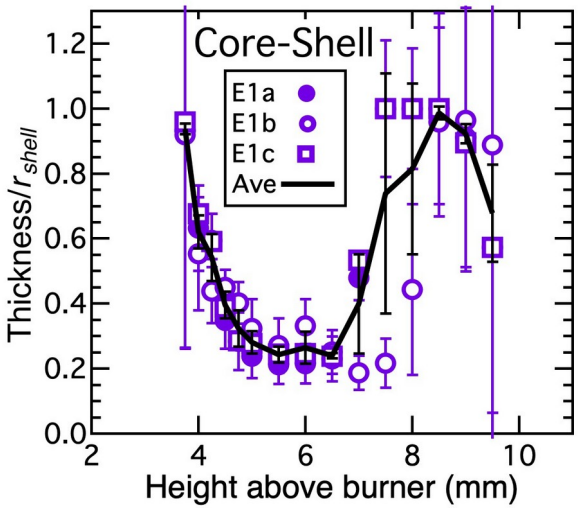

Figure 7. Ratio of primary-particle shell thickness to the particle radius. Results shown are from the single-mode fractal core-shell model. Error bars on the symbols represent the standard deviation of the fits (symbols) and the standard deviation of the mean (line).

Collectively, these results indicate that, in the center of the flame (4.25-7.5 mm), the primary particles have either (1) rough surfaces on the length scale of the primary-particle size, (2) smooth surfaces with some necking between primary particles in the aggregates, and/or (3) a measurable core-shell structure. At HABs greater than 7.5 mm, P_s approaches 4; D_s decreases, and the particle becomes homogeneous as the thickness approaches one. These results suggest that (1) the particles become smoother as they lose their outer layers of graphene during oxidation, (2) oxidation removes the overlayers of carbon largely responsible for necking between particles, and/or (3) oxidation removes outer layers of the primary particles leading to loss of the core-shell structure. Any of these explanations is consistent with previous results indicating that oxidation occurs on the surface of the primary particles at these locations in this flame [53] and with other previous results demonstrating that oxidation of mature soot particles proceeds at the particle surface at atmospheric pressure and high temperatures [105, 106].

At HABs between 4.0 and 4.75 mm, the power-law parameter for the primary particles decreases with increasing HAB, from $P_s = 4$ at 4.0 mm to $P_s = 3.48$ at 4.75 mm. At these HABs, the primary particles are expected to be increasing in maturity, losing hydrogen, and undergoing carbonization, becoming more graphitic and more dense with increasing HAB [53]. In addition, the particles are growing by surface addition, but the surface is maturing more slowly than the particle interior [53]. Such a difference between the particle bulk and surface layers is consistent with the decrease in P_s in this flame region. The change in density may also explain the dramatic

differences demonstrated between TEM images of particles extracted at HABs of 4 mm (Fig. 5b) and 5 mm (Fig. 5c). Coagulation of hydrocarbon particles, either in the flame or during extraction, may lead to the blobby structures observed for particles extracted at 4 mm. After the particles undergo carbonization and graphitization as part of the maturation process, collisions between more mature particles lead to agglomeration and aggregation. By the time the particles reach 5 mm, they appear as dendritic aggregates characteristic of mature soot particles (Fig. 5c).

4.5 Volume fraction. The results of the volume-fraction calculation for the unified-fit model are shown in Fig. 8a. Volume fractions are expressed in units of ppb, which represents the volume of the particles per unit volume in the flame such that 1 ppb = 1×10^{-9} cm^3 particle/cm^3 flame. We used values of the dispersion exponent ξ inferred from LII measurements between HABs of 4 and 9 mm [53] and Eqs. (16) – (21) to estimate volume fractions at these HABs. To estimate volume fractions at HABs larger than 9 mm, we used the average value of ξ measured between 5 and 9 mm (0.904). At HABs below 4 mm, we used a linear equation for ξ that gave reasonable values for both ξ and the C/H ratio low in the flame, i.e.

$$\xi(\mathrm{HAB} < 4\,\mathrm{mm}) = 5.4 - 1.1\,\mathrm{HAB}\,. \qquad (48)$$

At an HAB of 3 mm, this equation yields values for ξ of 2.1 and the C/H ratio of 1.8, which are consistent with previous measurements of immature soot particles observed at low HABs [117-119]. Volume fractions using Eq. (44) for the fractal core-shell model are shown in Fig. 8b.

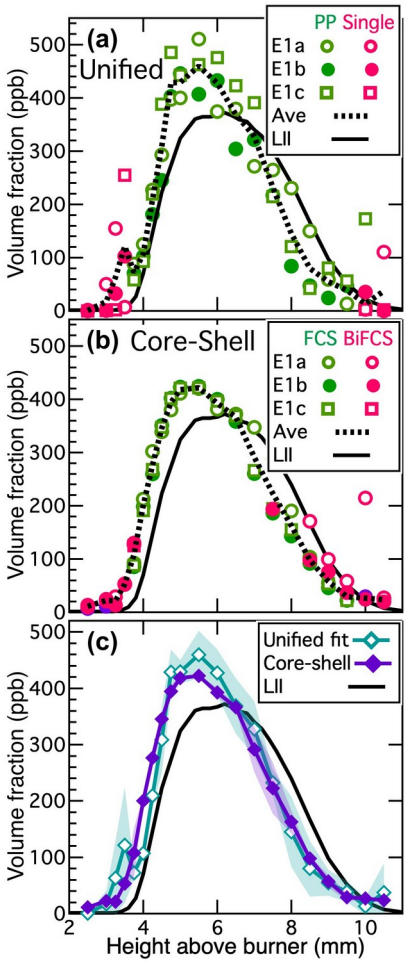

Figure 8. Volume fractions derived from fits to scattering profiles. Results are shown for the (a) unified model and (b) fractal core-shell model from fits to three flame datasets assuming either two modes (green points) or assuming a single mode (pink symbols). A comparison of the two models is shown in (c). The dotted black lines in (a) and (b) and the solid lines with symbols in (c) represent the averages of the fits, and the solid black lines show the results from LII measurements [52, 53]. The shading in (c) represents one σ standard deviation of the mean values. The accuracy of the LII measurements is estimated to be 17% [52].

These results are compared with the values derived using LII in all panels of Fig. 8 and with each other in Fig. 8c. The instrument calibration constant *C* was not measured directly. Estimates for this constant were derived by isolating the temperature-dependent gas-phase signal from the

temperature-independent instrument function at high q values in regions of the flame without soot [56]. Values derived from data taken on different days were in the range of 3.545 – 10.28 $\times$ 10^5. We assumed a value for the unified-model results of 1.028 $\times$ 10^6, and a value for the fractal core-shell results of 3.858 $\times$ 10^5. These values yield the same total volume fraction over the HAB range of 2.5-10.5 mm for the two models and are within the range of C values derived from analysis of the gas-phase data given by Michelsen *et al*. [56]. As shown in Eq. (16) and Eq. (44), this constant is in the denominator of the equation for volume fraction; thus, for the same value of C, the volume fraction from the unified model is larger than that from the fractal core-shell model by a factor ~2.7. With these scaling factors, the values of volume fraction yielded by the two models and the LII measurements are within 1.6% of one another at an HAB of 6.5 mm. Despite the difference in scaling between the two retrieval methods, the trends in volume fraction yielded by the models are consistent with each other.

The SAXS measurements demonstrate significantly higher signal at lower HAB values than do the LII measurements. This difference at lower HABs is likely attributable to soot maturity. LII is sensitive to soot only after it has undergone significant aging and graphitization, has strong absorption at visible and mid-infrared wavelengths, and is refractory and can reach higher temperatures. SAXS, on the other hand, should produce signal from very young particles to which LII has little sensitivity. At HABs where oxidation occurs, volume fractions inferred from LII measurements are larger than those from SAXS data. The lack of measurements at small enough q values to simulate aggregates accurately may introduce uncertainties in the volume fractions inferred from SAXS measurements. In addition, the SAXS measurements lacked an instrument calibration for these experiments; deriving C from gas-phase scattering leads to

systematic uncertainties in the absolute magnitude of the SAXS volume-fraction curve. Overall, our results suggest that LII and SAXS are a good complement for studying soot evolution.

Figure 9 shows the average of the volume-fraction data presented in Fig. 8 plotted as a function of temperature in the flame. Soot inception and maturation temperatures are extremely difficult to measure because many probes perturb the flame conditions, including temperature [120-131] and radical species concentrations [120-123, 132, 133]. Such perturbations can have dramatic effects on particle characteristics [128, 134-136]. The *in situ* techniques employed in this study provide an opportunity to measure temperatures and gain insight into particle characteristics without such perturbations.

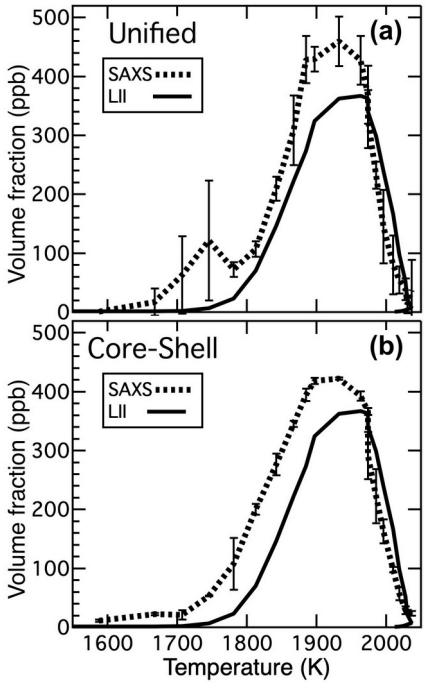

Figure 9. Soot volume fraction as a function of temperature. Results are shown for the (a) unified model and (b) fractal core-shell model. The dotted lines represent the average of the SAXS fits (same dotted lines as shown in Fig. 8) with error bars that represent one σ standard deviation of the mean, and the solid lines show the results from LII measurements [52, 53].

The SAXS measurements are valuable because they allow measurements of particles not mature enough to be detectable using LII and thus provide information about early soot formation. Figure 9 shows that SAXS signal from particles is first observed at a temperature of 1590 K. Our results indicate an upper limit on the temperature onset of inception, i.e., that inception occurs at temperatures of $\leq$ 1590 K. Previous measurements with thermocouples and extractive sampling of particles have suggested inception temperatures in the range of 900 - 1700 K [13, 137-141].

The onset of LII signal, on the other hand, occurs at a temperature of 1700 K, as shown in Fig. 9. Because LII is only sensitive to particles that are at least partially mature, this result suggests that particles start to mature at a temperature of ~1700 K. Future work will be required to quantify the difference between inception and maturation temperatures with the aim of developing an understanding of the processes that proceed between inception and maturation.

5. SUMMARY AND CONCLUSIONS

Soot SAXS signals were fit using a two-mode unified model and a fractal core-shell model. The results from the two models provide consistent qualitative information. When combined with complementary laser-based *in situ* diagnostics, the SAXS measurements provide a powerful means for gaining insight into particle inception, growth, chemical evolution, and oxidation.

A summary of the results is shown in Fig. 10. Fits using the two models demonstrate large monomer formation and an additional small-monomer mode at low HABs (2.5 – ~3.75 mm). The fractal core-shell model indicates that these particles have a uniform internal structure. A uniform internal structure is consistent with the results of the unified model, which indicates that they have smooth surfaces. These results are consistent with TEM images of large smooth blobby structures, XPS results of chemical disorder [53], and lack of LII signal [52, 53],

suggesting young non-refractory particles with negligible absorption cross sections at visible and near-IR wavelengths. Both models demonstrate an increase in volume fraction with HAB starting at 3.5 mm, accompanied by an increase in primary-particle size and aggregate size. Both models suggest that primary particles start to grow at HABs slightly lower (~0.25 mm) than that at which aggregates are formed. Between HABs of 4.25 and ~7.0 mm, the fractal core-shell model fits yield a core-shell structure, and those of the unified model yield a surface-fractal structure for the primary particles. These results are consistent with LII measurements demonstrating that the particles become mature and graphitic in this region of the flame [53]. Oxidation leads to a decrease in volume fraction and primary-particle size with HAB, starting at ~5.5 mm for both models. At large HABs (≥ 7.5 or 8.0 mm), the core-shell model indicates that the particles are internally uniform, and the unified model indicates that the particle surfaces are smooth. These results are consistent with XPS measurements demonstrating surface oxidation of the particles in this HAB range.

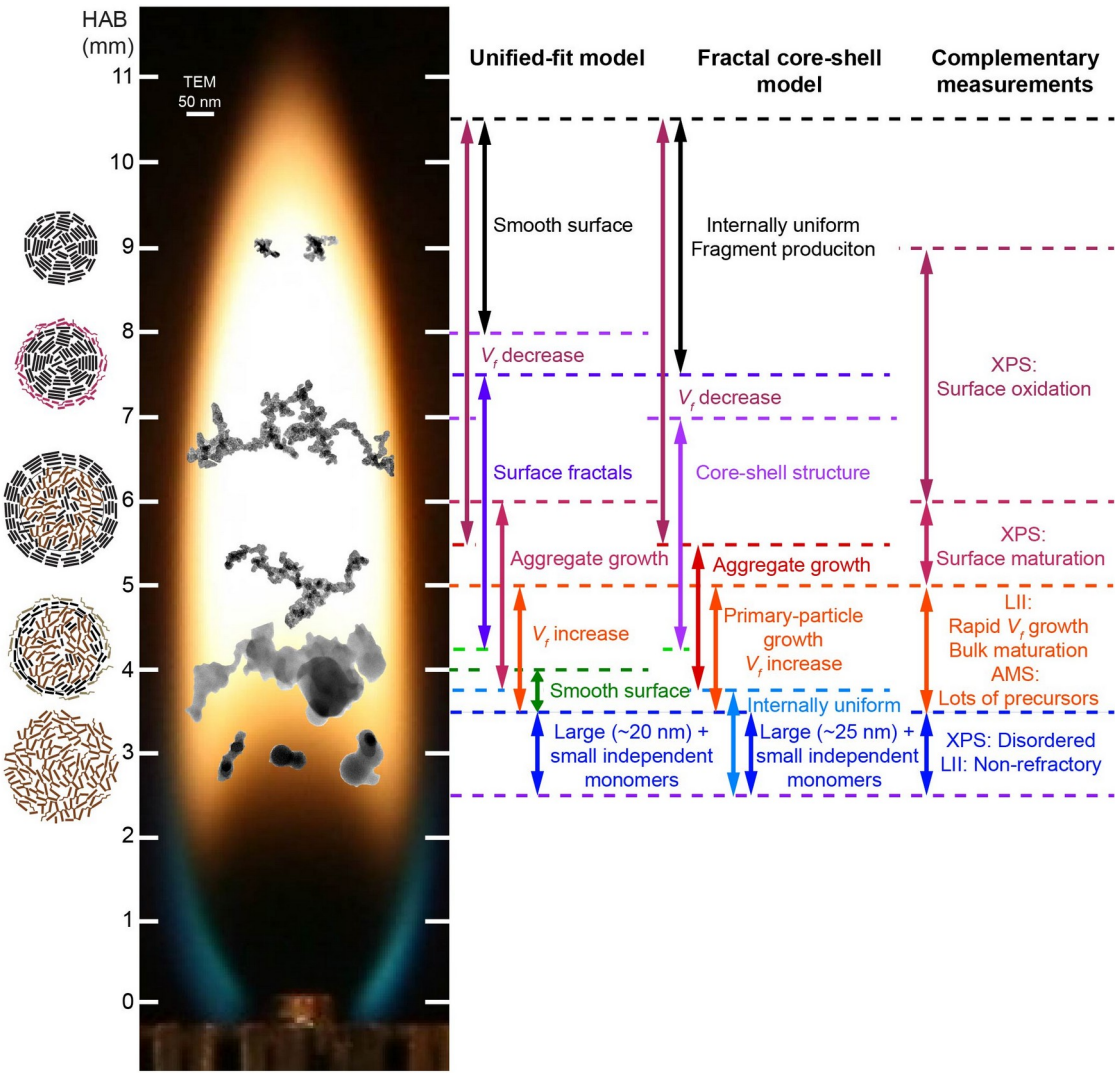

Figure 10. Summary of results of the unified model and fractal core-shell model. TEM images of representative particles are shown overlaid on a photo of the flame. Each particle image is shown at the HAB from which the particle was extracted. Corresponding summaries are shown to the right of the flame photo for results of the unified model, the fractal core-shell model, and previous experiments. Illustrations on the left side of the flame photo show schematic representations of primary particles that are consistent with the summary of results provided on the right side.

Primary-particle size distributions from the fractal core-shell model demonstrate excellent agreement with TEM size distributions throughout most of the flame (HABs ~5 - ~7 mm). In the region of the flame where particles are significantly oxidized (HABs above 7 mm), fits using the fractal core-shell model indicate the appearance of a small mode with a median diameter of ~2 nm, suggestive of particle fragmentation during oxidation. Particle-size distributions derived from unified-model results are consistently smaller than those extracted from TEM data. Median sizes derived using the unified model are 26 ± 6% smaller than those from TEM data over the HAB range of 5 – 7 mm.

The analysis also demonstrates that SAXS-inferred volume fractions reach a maximum at a lower height in the flame than do LII measurements. This result demonstrates sensitivity of X-ray scattering to young, internally disordered, hydrocarbon particles to which LII lacks sensitivity and highlights the value of combining these complementary techniques for studies of soot evolution in flames. The SAXS analysis, combined with the CARS temperature measurements, demonstrates that particle inception occurs at temperatures $\leq$ 1590 K. The combined SAXS, LII, and CARS analysis shows that soot starts to mature at ~1700 K.

We have developed a new model for analyzing SAXS data recorded on aggregates of core-shell particles. This model provides reliable fits that yield information about core-shell structure. The results are consistent with complementary measurements. In comparisons with the unified model, the fractal core-shell model demonstrates better agreement with TEM particle-size distributions and better precision in retrieved parameters, such as radius of gyration and volume fraction, and requires one fewer fitting parameter for most conditions. Reducing uncertainties can be achieved, particularly for aggregate parameters, by recording data over a wider q range that

includes smaller values of q, and, for volume fraction measurements, by measuring an instrument calibration function.

ASSOCIATED CONTENT

Supporting Information. The following files are available free of charge.

Descriptions of TEM analysis (SootRetrievals_2021_V1_SM.docx)

Scattering data used in the analysis for Flame E1a (CISoot_E1a_HAB02mm.xlsx, CISoot_E1a_HAB02mm.txt) and associated uncertainties (second sheet of CISoot_E1a_HAB02mm.xlsx, CISoot_E1a_HAB02mm_err.txt).

Scattering data used in the analysis for Flame E1b (CISoot_E1b_HAB02mm.xlsx, CISoot_E1b_HAB02mm.txt) and associated uncertainties (second sheet of CISoot_E1b_HAB02mm.xlsx, CISoot_E1b_HAB02mm_err.txt).

Scattering data used in the analysis for Flame E1c (CISoot_E1c_HAB02mm.xlsx, CISoot_E1c_HAB02mm.txt) and associated uncertainties (second sheet of CISoot_E1c_HAB02mm.xlsx, CISoot_E1c_HAB02mm_err.txt).

Author Contributions

The manuscript was written through contributions of all authors. AV, ICT, and HAM conceived of the experiments. MFC, RPB, PES, and HAM designed and constructed the flame apparatus. CZ and ES setup the SAXS beamline. ICT, AV, MFC, KOJ, PES, RPB, and HAM collected the SAXS data. HAM, MFC, and JAH analyzed the SAXS data. KOJ and PES collected the TEM data. EC, RPB, HAM, and KOJ analyzed the TEM data. HAM wrote the paper. All authors have given approval to the final version of the manuscript.

Funding Sources

HAM, MFC, KOJ, and PES were supported by the Division of Chemical Sciences, Geosciences, and Biosciences, the Office of Basic Energy Sciences, the U. S. Department of Energy (DOE). HAM was supported by DOE as part of the Gas-Phase Chemical Physics Program under a sub-contract from Sandia National Laboratories (FWP 22-022187) and was also supported by the College of Engineering and Applied Sciences at the University of Colorado Boulder. RPB was supported by the Sandia Laboratory Directed Research and Development (LDRD) Program. AV, ICT, and JAH were supported by the Lawrence Livermore National Laboratory (LLNL) under contract DE-AC52-07NA27344 and funded by the LDRD Program at LLNL under project tracking code 14-ERD-067. This research used resources of the Advanced Light Source, which is a DOE Office of Science User Facility under Contract no. DE-AC02-05CH11231. Sandia National Laboratories is a multi-mission laboratory managed and operated by National Technology & Engineering Solutions of Sandia, LLC, a wholly owned subsidiary of Honeywell International Inc., for the DOE's National Nuclear Security Administration under Contract DE-NA0003525. The views expressed in the article do not necessarily represent the views of the DOE or the United States Government.

Declaration of Competing Interest

We declare that we have no known competing financial interest or personal relationships that could appear to influence the work reported in this paper.

ACKNOWLEDGMENTS

We thank Jonathan Silberstein for assistance with running some of the preliminary fits. HAM, MFC, KOJ, and PES were supported by the Division of Chemical Sciences, Geosciences, and Biosciences, the Office of Basic Energy Sciences, the U. S. Department of Energy (DOE). HAM was supported by DOE as part of the Gas-Phase Chemical Physics Program under a sub-contract from Sandia National Laboratories (FWP 21-022187) and was also supported by the College of Engineering and Applied Sciences at the University of Colorado Boulder. RPB was supported by the Sandia Laboratory Directed Research and Development (LDRD) Program. AV, ICT, and JAH were supported by the Lawrence Livermore National Laboratory (LLNL) under contract DE-AC52-07NA27344 and funded by the LDRD Program at LLNL under project tracking code 14-ERD-067. This research used resources of the Advanced Light Source, which is a DOE Office of Science User Facility under Contract no. DE-AC02-05CH11231. Sandia National Laboratories is a multi-mission laboratory managed and operated by National Technology & Engineering Solutions of Sandia, LLC, a wholly owned subsidiary of Honeywell International Inc., for the DOE's National Nuclear Security Administration under Contract DE-NA0003525. The views expressed in the article do not necessarily represent the views of the DOE or the United States Government.

ABBREVIATIONS

SAXS, small-angle X-ray scattering; TEM, transmission electron microscopy; LII, laser-induced incandescence; HAB, height above the burner; CARS, coherent anti-Stokes Raman spectroscopy; XPS, X-ray photoelectron spectroscopy; SLM, standard (0°C, 1 atm) liters per

minute; PAH, polycyclic aromatic hydrocarbon; SANS, small-angle neutron scattering; DOE, U. S. Department of Energy.

REFERENCES

[1] C.A. Pope, D.W. Dockery, Health effects of fine particulate air pollution: Lines that connect, J. Air Waste Manage. 56(6) (2006) 709-742.
[2] M.R. Heal, P. Kumar, R.M. Harrison, Particles, air quality, policy and health, Chem. Soc. Rev. 41(19) (2012) 6606-6630.
[3] J.S. Lighty, J.M. Veranth, A.F. Sarofim, Combustion aerosols: Factors governing their size and composition and implications to human health, J. Air Waste Manage. 50(9) (2000) 1565-1618.
[4] R. Niranjan, A.K. Thakur, The toxicological mechanisms of environmental soot (black carbon) and carbon black: Focus on oxidative stress and inflammatory pathways, Frontiers in Immunology 8 (2017) 763.
[5] H.J. Heusinkveld, T. Wahle, A. Campbell, R.H.S. Westerink, L. Tran, H. Johnston, V. Stone, F.R. Cassee, R.P.F. Schins, Neurodegenerative and neurological disorders by small inhaled particles, NeuroToxiology 56 (2016) 94-106.
[6] T.C. Bond, S.J. Doherty, D.W. Fahey, P.M. Forster, T. Berntsen, B.J. DeAngelo, M.G. Flanner, S. Ghan, B. Kärcher, D. Koch, S. Kinne, Y. Kondo, P.K. Quinn, M.C. Sarofim, M.G. Schultz, M. Schulz, C. Venkataraman, H. Zhang, S. Zhang, N. Bellouin, S.K. Guttikunda, P.K. Hopke, M.Z. Jacobson, J.W. Kaiser, Z. Klimont, U. Lohmann, J.P. Schwarz, D. Shindell, T. Storelvmo, S.G. Warren, C.S. Zender, Bounding the role of black carbon in the climate system: A scientific assessment, J. Geophys. Res. 118(11) (2013) 5380-5552.
[7] IPCC, Climate change 2013: The physical science basis. Working group I Contribution to the fifth assessment report of the intergovernmental panel on climate change, Cambridge University Press, Cambridge, UK and New York, NY, 2013.
[8] A.D. Abid, E.D. Tolmachoff, D.J. Phares, H. Wang, Y. Liu, A. Laskin, Size distribution and morphology of nascent soot in premixed ethylene flames with and without benzene, Proc. Combust. Inst. 32(1) (2009) 681-688.
[9] L.A. Sgro, G. Basile, A.C. Barone, A. D'Anna, P. Minutolo, A. Borghesi, A. D'Alessio, Detection of combustion formed nanoparticles, Chemosphere 51 (2003) 1079-1090.
[10] A. D'Anna, A. Rolando, C. Allouis, P. Minutolo, A. D'Alessio, Nano-organic carbon and soot particle measurements in a laminar ethylene diffusion flame, Proc. Combust. Inst. 30 (2005) 1449-1456.
[11] A.C. Barone, A. D'Alessio, A. D'Anna, Morphological characterization of the early process of soot formation by atomic force microscopy, Combust. Flame 132 (2003) 181-187.
[12] A. D'Anna, M. Commodo, S. Violi, C. Allouis, J.H. Kent, Nano organic carbon and soot in turbulent non-premixed ethylene flames, Proc. Combust. Inst. 31(1) (2007) 621-629.
[13] H. Wang, Formation of nascent soot and other condensed-phase materials in flames, Proc. Combust. Inst. 33 (2011) 41-67.
[14] H.A. Michelsen, Probing soot formation, chemical and physical evolution, and oxidation: A review of in situ diagnostic techniques and needs, Proc. Combust. Inst. 36(1) (2017) 717-735.

[15] H.A. Michelsen, M.B. Colket, P.-E. Bengtsson, A. D'Anna, P. Desgroux, B.S. Haynes, J.H. Miller, G.J. Nathan, H. Pitsch, H. Wang, A review of terminology used to describe soot formation and evolution under combustion and pyrolytic conditions, ACS Nano 14 (2020) 12470-12490.
[16] R.L. Vander Wal, V.M. Bryg, C.-H. Huang, Aircraft engine particulate matter: Macro-micro- and nanostructure by HRTEM and chemistry by XPS, Combust. Flame 161(2) (2014) 602-611.
[17] R.A. Dobbins, C.M. Megaridis, Morphology of flame-generated soot as determined by thermophoretic sampling, Langmuir 3(2) (1987) 254-259.
[18] R. Puri, T.F. Richardson, R.J. Santoro, R.A. Dobbins, Aerosol dynamic processes of soot aggregates in a laminar ethene diffusion flame, Combust. Flame 92(3) (1993) 320-333.
[19] J.-O. Müller, D.S. Su, U. Wild, R. Schlögl, Bulk and surface structural investigations of diesel engine soot and carbon black, Phys. Chem. Chem. Phys. 9(30) (2007) 4018-4025.
[20] T. Ishiguro, Y. Takatori, K. Akihama, Microstructure of diesel soot particles probed by electron microscopy: First observation of inner core and outer shell, Combust. Flame 108 (1997) 231-234.
[21] A. La Rocca, F. Bonatesta, M.W. Fay, F. Campenella, Characterisation of soot in oil from a gaseline direct injection engine using transmission electron microscopy, Tribol. Int. 86 (2015) 77-84.
[22] M. Alfè, B. Apicella, R. Barbella, J.N. Rouzaud, A. Tregrossi, A. Ciajolo, Structure–property relationship in nanostructures of young and mature soot in premixed flames, Proc. Combust. Inst. 32(1) (2009) 697-704.
[23] P. Toth, A.B. Palotas, T.A. Ring, E.G. Eddings, R.L. Vander Wal, J.S. Lighty, The effect of oxidation pressure on the equilibrium nanostructure of soot particles, Combust. Flame 162 (2015) 2422-2430.
[24] L.B. Ebert, J.C. Scanlon, C.A. Clausen, Combustion tube soot from a Diesel fuel/air mixture: Issues in structure and reactivity, Energy Fuels 2 (1988) 438-445.
[25] R.L. Vander Wal, A TEM methodology for the study of soot particle structure, Combust. Sci. Technol. 126 (1997) 333-357.
[26] R.L. Vander Wal, Soot precursor carbonization: Visualization using LIF and LII and comparison using bright and dark field TEM, Combust. Flame 112 (1998) 607-616.
[27] R.H. Muñoz, T.T. Charalampopoulos, Evolution of compositional and structural properties of soot in premixed alkane flames, Twenty-Seventh Symposium (International) on Combustion 27(1) (1998) 1471-1479.
[28] Y. Zhang, A.L. Boehman, Oxidation behavior of soot generated from the combustion of methyl 2-butenoate in a co-flow diffusion flame, Combust. Flame 160(1) (2013) 112-119.
[29] W.A. England, An *in situ* X-ray small angle scattering study of soot morphology in flames, Combust. Sci. Technol. 46(1-2) (1986) 83-93.
[30] J.P. Hessler, S. Seifert, R.E. Winans, Spatially resolved small-angle x-ray scattering studies of soot inception and growth, Proc. Combust. Inst. 29(2) (2002) 2743-2748.
[31] J.P. Hessler, S. Seifert, R.E. Winans, T.H. Fletcher, Small-angle X-ray studies of soot inception and growth, Faraday Discuss. 119(1) (2001) 395-407.
[32] C. Gardner, G.N. Greaves, G.K. Hargrave, S. Jarvis, P. Wildman, F. Meneau, W. Bras, G. Thomas, *In situ* measurements of soot formation in simple flames using small angle X-ray scattering, Nucl. Instrum. Meth. B 238(1-4) (2005) 334-339.

[33] J.B.A. Mitchell, J. Courbe, A.I. Florescu-Mitchell, S. di Stasio, T. Weiss, Demonstration of soot particle resizing in an ethylene flame by small angle x-ray scattering, J. Appl. Phys. 100(12) (2006) 124918.
[34] S. di Stasio, J.B.A. Mitchell, J.L. LeGarrec, L. Biennier, M. Wulff, Synchrotron SAXS in situ identification of three different size modes for soot nanaoparticles in a diffusion flame, Carbon 44 (2006) 1267-1279.
[35] M. Sztucki, T. Narayanan, G. Beaucage, *In situ* study of aggregation of soot particles in an acetylene flame by small-angle x-ray scattering, J. Appl. Phys. 101(11) (2007) 114304.
[36] J.B.A. Mitchell, S. di Stasio, J.L. LeGarrec, A.I. Florescu-Mitchell, Synchrotron radiation studies of additives in combustion I: Water, Nucl. Instrum. Meth. B 268(9) (2010) 1486-1491.
[37] J.B.A. Mitchell, S. di Stasio, J.L. LeGarrec, A.I. Florescu-Mitchell, T. Narayanan, M. Sztucki, Small angle x-ray scattering study of flame soot nanoparticle aggregation and restructuring, J. Appl. Phys. 105(12) (2009) 124904.
[38] L. Vallenhag, S.E. Canton, P. Sondhauss, D. Haase, F. Ossler, A combined small- and wide-angle x-ray scattering detector for measurements on reactive systems, Rev. Sci. Instrum. 82(8) (2011) 083104.
[39] S. di Stasio, J.L. LeGarrec, J.B.A. Mitchell, Synchrotron radiation studies of additives in combustion, II: Soot agglomerate microstructure change by alkali and alkaline-earth metal addition to a partially premixed flame, Energy Fuels 25(3) (2011) 916-925.
[40] J.B.A. Mitchell, J.L. LeGarrec, S. di Stasio, X-ray studies of combustion generated nanostructures, AIP Conf. Proc. 1370(1) (2011) 47-53.
[41] J.B.A. Mitchell, J.L. LeGarrec, G. Saidani, F. Lefeuvre, S. di Stasio, Synchrotron Radiation Studies of Additives in Combustion, III: Ferrocene, Energy Fuels 27(8) (2013) 4891-4898.
[42] F. Ossler, L. Vallenhag, S.E. Canton, J.B.A. Mitchell, J.-L. Le Garrec, M. Sztucki, S. di Stasio, Dynamics of incipient carbon particle formation in a stabilized ethylene flame by *in situ* extended-small-angle- and wide-angle X-ray scattering, Carbon 51 (2013) 1-19.
[43] S. di Stasio, Soot with 10^{13} cm^{-3} high concentration and 25 Å radius of gyration as detected by small-angle X-ray scattering in a premixed ethylene-air flame at sooting threshold, J. Aerosol Sci. 110 (2017) 11-24.
[44] F. Zhang, C. Wang, W. Han, Y. Zou, J. Wang, S. Seifert, R.E. Winans, Soot formation and growth with palladium acetylacetonate-toluene injection in ethylene base flames investigated by *in situ* synchrotron small-angle X-ray scattering, Proc. Combust. Inst. 38 (2021) 1859-1866.
[45] M. Bagge-Hanson, S. Bastea, J.A. Hammons, M. Nielsen, L.M. Lauderbach, R.L. Hodgin, P. Pagoria, C. May, S. Aloni, A. Jones, W.L. Shaw, E.V. Bukovsky, N. Sinclair, R.L. Gustavsen, E.B. Watkins, B.J. Jensen, D.M. Dattelbaum, M.A. Firestone, R.C. Huber, B.S. Ringstrand, J.R.I. Lee, T. van Buuren, L.E. Fried, T.M. Willey, Detonation synthesis of carbon nano-onions via liquid carbon condensation, Nature Communications 10 (2019) 3819.
[46] J.A. Hammons, M. Nielsen, M. Bagge-Hanson, S. Bastea, W.L. Shaw, J.R.I. Lee, J. Ilavsky, N. Sinclair, K. Fezzaa, L.M. Lauderbach, R.L. Hodgin, D.A. Orlikowski, L.E. Fried, T.M. Willey, Resolving detonation danodiamond size evolution and morphology at sub-microsecond timescales during high-explosive detonations, The Journal of Physical Chemistry C 123 (2019) 19153-19164.
[47] J.A. Hammons, M. Nielsen, M. Bagge-Hanson, L.M. Lauderbach, R.L. Hodgin, S. Bastea, L.E. Fried, M.R. Cowan, D.A. Orlikowski, T.M. Willey, Observation of variations in condensed

carbon morphology dependent on Composition B detonation conditions, Propellants, Explosives, Pyrotechnics 45 (2020) 347-355.
[48] X. Tang, C. Wang, F. Zhang, Q. Wang, J. Wang, S. Seifert, R.E. Winans, Effect of nickel acetylacetonate addition on soot inception and growth in an ethylene flame studied by using in situ small-angle X-ray scattering, Combust. Flame 206 (2019) 390-399.
[49] G. Beaucage, Approximations leading to a unified exponential/power-law approach to small-angle scattering, J. Appl. Crystallogr. 28(6) (1995) 717-728.
[50] G. Beaucage, D.W. Schaefer, Structural studies of complex systems using small-angle scattering: A unified Guinier/power-law approach, Journal of Non-Crystalline Solids 172-174 (1994) 797-805.
[51] G. Beaucage, Small-Angle Scattering from Polymeric Mass Fractals of Arbitrary Mass-Fractal Dimension, J. Appl. Crystallogr. 29(2) (1996) 134-146.
[52] M.F. Campbell, A. Bohlin, P.E. Schrader, R.P. Bambha, C.J. Kliewer, K.O. Johansson, H.A. Michelsen, Design and characterization of a linear Hencken-type burner, Rev. Sci. Instrum. 87(11) (2016) 115114.
[53] K.O. Johansson, F. El Gabaly, P.E. Schrader, M.F. Campbell, H.A. Michelsen, Evolution of maturity levels of particle surface and bulk during soot growth and oxidation in a flame, Aerosol Sci. Tech. 51(12) (2017) 1333-1344.
[54] R. Besselink, T.M. Stawski, A.E.S. Van Driessche, L.G. Benning, Not just fractal surfaces, but surface fractal aggregates: Derivation of the expression for the structure factor and its applications, J. Chem. Phys. 145 (2016) 211908.
[55] A. Hexemer, W. Bras, J. Glossinger, E. Schaible, E. Gann, R. Kirian, A. MacDowell, M. Church, B. Rude, H. Padmore, A SAXS/WAXS/GISAXS beamline with multilayer monochromator, J. Phys. Conf. Ser. 247 (2010) 012007.
[56] H.A. Michelsen, M.F. Campbell, I.C. Tran, K.O. Johansson, P.E. Schrader, R.P. Bambha, J.A. Hammons, E. Schaible, C. Zhu, T. van Buuren, Distinguishing gas-phase and nanoparticle contributions to small-angle scattering in X-ray scattering reacting aerosol flows, Journal of Physical Chemistry A (2022) in press.
[57] P.M. Anderson, H. Guo, P.B. Sunderland, Repeatability and reproducibility of semi-automated measurements of soot primary particle size sistributions from TEM images, J. Aerosol Sci. 114 (2017) 317-326.
[58] WaveMetrics, Igor Pro, Lake Oswego, OR, USA.
[59] J.M. Headrick, P.E. Schrader, H.A. Michelsen, Radial-profile and divergence measurements of combustion-generated soot focused by an aerodynamic-lens system, J. Aerosol Sci. 58 (2013) 158-170.
[60] A.M. Brasil, T.L. Farias, M.G. Carvalho, Ü.Ö. Köylü, Numerical characterization of the morphology of aggregated particles, J. Aerosol Sci. 32(4) (2001) 489-508.
[61] A.M. Brasil, T.L. Farias, M.G. Carvalho, A recipe for image characterization of fractal-like aggregates, J. Aerosol Sci. 30(10) (1999) 1379-1389.
[62] C. Oh, C.M. Sorensen, The effect of overlap between monomers on the determination of fractal cluster morphology, J. Colloid Interf. Sci. 193(1) (1997) 17-25.
[63] J. Ilavsky, Nika: software for two-dimensional data reduction, J. Appl. Crystallogr. 45(2) (2012) 324-328.

[64] G. Beaucage, S. Rane, S. Sukumaran, M.M. Satkowski, L.A. Schechtman, Y. Doi, Persistence length of isotactic poly(hydroxy butyrate), Macromolecules 30(14) (1997) 4158-4162.
[65] J. Hyeon-Lee, G. Beaucage, S.E. Pratsinis, S. Vemury, Fractal analysis of flame-synthesized nanostructured silica and titania powders using small-angle X-ray scattering, Langmuir 14 (1998) 5751-5756.
[66] A. Guinier, G. Fournet, Small-Angle Scattering of X-Rays, John Wiley & Sons, Inc., New York, 1955.
[67] L. Ma, H. Yong, J.D. Geiser, A.M. Carrascosa, N. Goff, P.M. Weber, Ultrafast x-ray and electron scattering of free molecules: A comparative evaluation, Struct. Dyn. 7 (2020) 034102.
[68] P. Willmott, An Introduction to Synchrotron Radiation, 2nd ed., Wiley, Hoboken, NJ, 2019.
[69] L.A. Feigin, D.I. Svergun, Structure Analysis by Small-Angle X-Ray and Neutron Scattering, Springer, New York, 1987.
[70] A. Guinier, X-ray Diffraction in Crystals, Imperfect Crystals, and Amorphous Bodies, W. H. Freeman, San Francisco, 1963.
[71] O.H. Seeck, B.M. Murphy, X-Ray Diffraction: Modern Experimental Techniques, Pan Stanford Publishing, Singapore, 2015, p. 427.
[72] A.J. Hurd, D.W. Schaefer, D.M. Smith, S.B. Ross, A. Le Méhauté, S. Spooner, Surface areas of fractally rough particles studied by scattering, Phys. Rev. B 39(13) (1989) 9742-9745.
[73] P.-Z. Wong, A.J. Bray, Small-angle scattering by rough and fractal surfaces, J. Appl. Crystallogr. 21 (1988) 786-794.
[74] G. Beaucage, Determination of branch fraction and minimum dimension of mass-fractal aggregates, Phys. Rev. E 70 (2004) 031401.
[75] K. Butter, A. Hoell, A. Wiedenmann, A.V. Petukhov, G.-J. Vroege, Small-angle neutron and X-ray scattering of dispersions of oleic-acid-coated magnetic iron particles, J. Appl. Crystallogr. 37 (2004) 847-856.
[76] H.A. Michelsen, Effects of Maturity and Temperature on Soot Density and Specific Heat, Proc. Combust. Inst. 38 (2021) 1197-1205
[77] M.M. Maricq, S.J. Harris, J.J. Szente, Soot size distributions in rich premixed ethylene flames, Combust. Flame 132(3) (2003) 328-342.
[78] B. Zhao, K. Uchikawa, H. Wang, A comparative study of nanoparticles in premixed flames by scanning mobility particle sizer, small angle neutron scattering, and transmission electron microscopy, Proc. Combust. Inst. 31(1) (2007) 851-860.
[79] H.M.F. Amin, A. Bennett, W.L. Roberts, Determining fractal properties of soot aggregates and primary particle size distribution in counterflow flames up to 10 atm, Proc. Combust. Inst. 37 (2019) 1161-1168.
[80] F. Patiño, J.J. Cruz, I. Verdugo, J. Morán, J.-L. Consalvi, F. Liu, X. Du, A. Fuentes, Soot primary particle sizing in a n-heptane doped methane/air laminar coflow diffusion flame by planar two-color TiRe-LII and TEM image analysis, Fuel 266 (2020) 117030.
[81] H. Chu, W. Han, W. Cao, C. Tao, M. Raza, L. Chen, Experimental investigation of soot morphology and primary particle size along axial and radial direction of an ethylene diffusion flame via electron microscopy, Journal of the Energy Institute 93(5) (2019) 1294-1302.
[82] G. Beaucage, H.K. Kammler, S.E. Pratsinis, Particle size distributions from small-angle scattering using global scattering functions, J. Appl. Crystallogr. 37(4) (2004) 523-535.

[83] S.J. Harris, A.M. Weiner, Chemical kinetics of soot particle growth, Annual Review of Physical Chemistry 36 (1985) 31-52.
[84] J.B. Howard, Carbon addition and oxidation reactions in heterogeneous combustion and soot formation, Proc. Combust. Inst. 23(1) (1990) 1107-1127.
[85] A. D'Alessio, A. D'Anna, A. D'Orsi, P. Minutolo, R. Barbella, A. Ciajolo, Precursor formation and soot inception in premixed ethylene flames, Symp. (Int.) Comb. 24(1) (1992) 973-980.
[86] R.A. Dobbins, H. Subramanian, Soot precursors: Particles in flames, in: H. Bockhorn (Ed.), Soot Formation in Combustion, Springer-Verlag, Berlin, 1994, pp. 290-301.
[87] A. Ciajolo, R. Barbella, A. Tregrossi, L. Bonfanti, Spectroscopic and compositional signatures of PAH-loaded mixtures in the soot inception region of a premixed ethylene flame, Proc. Combust. Inst. 27(1) (1998) 1481-1487.
[88] J. Li, S. Yu, Soot particles analysis in laminar premixed propane/oxygen (C_3H_8/O_2) flame using published measurement data, China Particuology 1(4) (2003) 168-171.
[89] C. Russo, A. Tregrossi, A. Ciajolo, Dehydrogenation and growth of soot in premixed flames, Proc. Combust. Inst. 35(2) (2015) 1803-1809.
[90] J. Teixeira, Small-angle scattering by fractal systems, J. Appl. Crystallogr. 21 (1988) 781-785.
[91] P. Bartlett, R.H. Ottewill, A neutron scattering study of the structure of a bimodal colloidal crystal, J. Chem. Phys. 96 (1992) 3306-3318.
[92] W.R. Heinson, C.M. Sorensen, A. Chakrabarti, A three parameter description of the structure of diffusion limited cluster fractal aggregates, J. Colloid Interf. Sci. 375 (2012) 65-69.
[93] M. Bonini, E. Fratini, P. Baglioni, SAXS study of chain-like structures formed by magnetic nanoparticles, Materials Science and Engineering C 27 (2007) 1377-1381.
[94] S.-H. Chen, J. Teixeira, Structure and fractal dimension of protein-detergent complexes, Phys. Rev. Lett. 57(20) (1986) 2583-2586.
[95] P.S. Goyal, V.K. Aswal, Combined SANS and SAXS in studies of nanoparticles with core-shell structure, Indian Journal of Pure and Applied Physics 44 (2006) 724-728.
[96] J.P. Hessler, R.S. Tranter, S. Vajda, N. Van Wersmekerken, Nucleation and growth and carbonaceous nano-sized particles, https://www.aps.anl.gov/sites/www.aps.anl.gov/files/APS-sync/activity_reports/apsar2003/HESSLER1.PDF, 2003.
[97] J. Yon, F.X. Ouf, D. Hebert, J.B.A. Mitchell, N. Teuscher, J.-L. Le Garrec, A. Bescond, W. Baumann, D. Ourdani, T. Bizien, J. Perez, Investigation of soot oxidation by coupling LII, SAXS and scattering measurements, Combust. Flame 190 (2018) 441-453.
[98] T. Nicolais, D. Durand, J.-C. Gimel, Static structure factor of dilute solutions of polydisperse fractal aggregates, Physical Review B: Condensed Matter 50(22) (1994) 16357-16363.
[99] C.D. Zangmeister, J.G. Radney, L.T. Dockery, J.T. Young, X. Ma, R. You, M.R. Zachariah, Packing density of rigid aggregates is independent of scale, P. Natl. Acad. Sci. USA 111(25) (2014) 9037-9041.
[100] K.G. Neoh, J.B. Howard, A.F. Sarofim, Effect of oxidation on the physical structure of soot, Twentieth Symposium (International) on Combustion 20 (1985) 951-957.
[101] C.A. Echavarria, I.C. Jaramillo, A.F. Sarofim, J.S. Lighty, Studies of soot oxidation and fragmentation in a two-stage burner under fuel-lean and fuel-rich conditions, Proc. Combust. Inst. 33 (2011) 659-666.

[102] M. Sirignano, J.H. Kent, A. D'Anna, Further experimental and modelling evidences of soot fragmentation in flames, Proc. Combust. Inst. 35 (2015) 1779-1786.
[103] H. Ghiassi, P. Toth, I.C. Jaramillo, J.S. Lighty, Soot oxidation-induced fragmentation: Part 1: The relationship between soot nanostructure and oxidation-induced fragmentation, Combust. Flame 163 (2016) 179-187.
[104] H. Ghiassi, I.C. Jaramillo, P. Toth, J.S. Lighty, Soot oxidation-induced fragmentation: Part 2: Experimental investigation of the mechanism of fragmentation, Combust. Flame 163 (2016) 170-178.
[105] A.D. Sediako, C. Soong, J.Y. Howe, M.R. Kholghy, M.J. Thomson, Real-time observation of soot aggregate oxidation in an Environmental Transmission Electron Microscope, Proc. Combust. Inst. 36(1) (2017) 841-851.
[106] P. Toth, D. Jacobsson, M. Ek, H. Wiinikka, Real-time, in situ, atomic scale observation of soot oxidation, Carbon 145 (2019) 149-160.
[107] S.R. Forrest, J. Witten, T. A., Long-range correlations in smoke-particle aggregates, Journal of Physics A: Mathematical and General 12(5) (1979) L109-L117.
[108] Ü.Ö. Köylü, G.M. Faeth, Structure of overfire soot in buoyant turbulent diffusion flames at long residence times, Combust. Flame 89(2) (1992) 140-156.
[109] Ü.Ö. Köylü, G.M. Faeth, T.L. Farias, M.G. Carvalho, Fractal and projected structure properties of soot aggregates, Combust. Flame 100(4) (1995) 621-633.
[110] T.T. Charalampopoulos, H. Chang, Agglomerate parameters and fractal dimension of soot using light scattering—effects on surface growth, Combust. Flame 87(1) (1991) 89-99.
[111] C.M. Sorensen, Light scattering by fractal aggregates: A review, Aerosol Sci. Tech. 35(2) (2001) 648-687.
[112] R.P. Bambha, M.A. Dansson, P.E. Schrader, H.A. Michelsen, Effects of volatile coatings and coating removal mechanisms on the morphology of graphitic soot, Carbon 61 (2013) 80-96.
[113] N. Lu, C.M. Sorensen, Depolarized light scattering from fractal soot aggregates, Phys. Rev. E 50(4) (1994) 3109-3115.
[114] J. Johnsson, H. Bladh, N.-E. Olofsson, P.-E. Bengtsson, Influence of soot aggregate structure on particle sizing using laser-induced incandescence: Importance of bridging between primary particles, Applied Physics B: Lasers and Optics 112(3) (2013) 321-332.
[115] J. Lahaye, F. Ehrburger-Dolle, Mechanisms of carbon black formation: Correlation with the morphology of aggregates, Carbon 32(7) (1994) 1319-1324.
[116] J. Wagner, Small-angle scattering from spherical core-shell particles: An analytical scattering function for particles with Schulz-Flory size distribution, J. Appl. Crystallogr. 37 (2004) 750-756.
[117] A. D'Alessio, F. Beretta, C. Venitozzi, Optical investigations of soot forming methane-oxygen flames, Combust. Sci. Technol. 5 (1972) 263-272.
[118] R.C. Millikan, Sizes, optical properties, and temperatures of soot particles, in: A.I. Dahl (Ed.), Applied Methods and Instruments, Litton Educational Pub., Inc.1962, pp. 497-507.
[119] R.C. Millikan, Optical properties of soot, Journal of the Optical Society of America 51(6) (1961) 698-699.
[120] J. Biordi, C.P. Lazzara, J.F. Papp, Molecular beam mass spectrometry applied to determining the kinetics of reactions in flames: 1. Empirical characterization of flame perturbation by molecular beam sampling probes, Combust. Flame 23(73-82) (1974) 73.

[121] O.I. Smith, D.W. Chandler, An experimental study of probe distortions to the structure of one-dimensional flames, Combust. Flame 63(19-29) (1986) 19.
[122] U. Struckmeier, P. Oßwald, T. Kasper, L. Böhling, M. Heusing, M. Köhler, A. Brockhinke, K. Kohse-Höinghaus, Sampling probe influences on temperature and species concentrations in molecular beam mass spectroscopi investigations of flat premixed low-pressure flames, Zeitschrift fuer Physikalische Chemie (Munich) 223(4-5) (2009) 503-537.
[123] L. Deng, A. Kempf, O. Hasemann, O.P. Korobeinichev, I. Wlokas, Investigation of the sampling nozzle effect on laminar flat flames, Combust. Flame 162 (2015) 1737-1747.
[124] P. Desgroux, L. Gasnot, J.F. Pauwels, L.R. Sochet, Correction of LIF temperature measurements for laser absorption and fluorescence trapping in a flame: Application to the thermal perturbation study induced by a sampling probe, Appl. Phys. B. 61 (1995) 401-407.
[125] A.D. Abid, J. Camacho, D.A. Sheen, H. Wang, Quantitative measurement of soot particle size distribution in premixed flames – The burner-stabilized stagnation flame approach, Combust. Flame 156(10) (2009) 1862-1870.
[126] A. De Filippo, L.A. Sgro, G. Lanzuolo, A. D'Alessio, Probe measurements and numerical model predictions of evolving size distributions in premixed flames, Combust. Flame 156 (2009) 1744-1754.
[127] C. Saggese, A. Cuoci, A. Frassoldati, S. Ferrariio, J. Camacho, H. Wang, T. Faravelli, Probe effects in soot sampling from a burner-stabilized stagnation flame, Combust. Flame 167 (2016) 184-197.
[128] M. Sirignano, A. D'Anna, Effect of sampling probe perturbation on particle size distribution functions in a slightly sooting premixed flame of ethylene: A modeling study, Combust. Sci. Technol. 184(7-8) (2012) 1011-1021.
[129] A.T. Hartlieb, B. Atakan, K. Kohse-Höinghaus, Effects of a sampling quartz nozzle on the flame structure of a fuel-rich low-pressure propene flame, Combust. Flame 121 (2000) 610-624.
[130] N. Hansen, M. Schenk, K. Moshammer, K. Kohse-Höinghaus, Investigating repetitive reaction pathways for the formation of polycyclic aromatic hydrocarbons in combustion processes, Combust. Flame 180 (2017) 250-261.
[131] N. Hansen, R.S. Tranter, J.B. Randazzo, J.P.A. Lockhart, A.L. Kastengren, Investigation of sampling-probe distorted temperature fields with X-ray fluorescence spectroscopy, Proc. Combust. Inst. 37 (2019) 1401-1408.
[132] E.L. Knuth, Composition distortion in MBMS sampling, Combust. Flame 103(3) (1995) 171-180.
[133] D. Stepowski, D. Puechberty, M.J. Cottereau, Use of laser-induced fluorescence of OH to study the perturbation of a flame by a probe, Proc. Combust. Inst. 18 (1981) 1567-1573.
[134] F.X. Ouf, J. Yon, P. Ausset, A. Coppalle, M. Maillé, Influence of sampling and storage protocol on fractal morphology of soot studied by transmission electron microscopy, Aerosol Sci. Tech. 44(11) (2010) 1005-1017.
[135] J. Lee, I. Altman, M. Choi, Design of thermophoretic probe for precise particle sampling, J. Aerosol Sci. 39 (2008) 418-431.
[136] E. Goudeli, A.J. Gröhn, S.E. Pratsinis, Sampling and dilution of nanoparticles at high temperature, Aerosol Sci. Tech. 50(6) (2016) 591-604.
[137] R.J. Santoro, T.T. Yeh, J.J. Horvath, H.G. Semerjian, The transport and growth of soot particles in laminar diffusion flames, Combust. Sci. Technol. 53(2-3) (1987) 89-115.

[138] A. Gomez, M.G. Littman, I. Glassman, Comparative study of soot formation on the centerline of axisymmetric laminar diffusion flames: Fuel and temperature effects, Combust. Flame 70 (1987) 225-241.
[139] K. Saito, A.S. Gordon, F.A. Williams, W.F. Stickle, A study of the early history of soot formation in various hydrocarbon diffusion flames, Combust. Sci. Technol. 80(1-3) (1991) 103-119.
[140] M.R. Kholghy, M. Saffaripour, C. Yip, M.J. Thomson, The evolution of soot morphology in a laminar coflow diffusion flame of a surrogate for Jet A-1, Combust. Flame 160 (2013) 2119-2130.
[141] X. Zhou, X. Liu, J.B. Jeffries, R.K. Hanson, Development of a sensor for temperature and water concentration in combustion gases using a single tunable diode laser, Meas. Sci. Technol. 14(8) (2003) 1459.

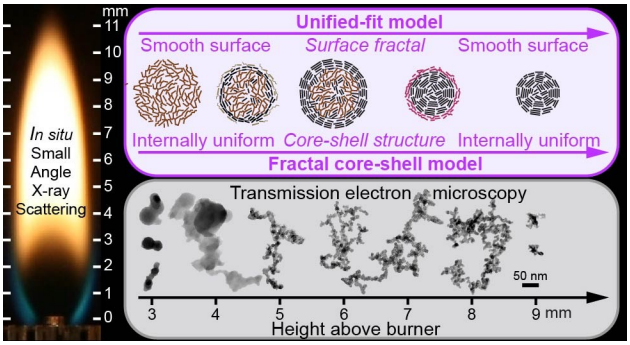

Table of Contents Graphic: New model for *in situ* small-angle X-ray scattering provides soot internal structure in a flame.